NASA Technical Memorandum 101726

In-Flight Flow Visualization with Pressure Measurements at Low Speeds on the NASA F-18 High Alpha Research Vehicle

John H. Del Frate, David F. Fisher, and Fanny A. Zuniga

October 1990

(NASA-TM-101726) IN-FLIGHT FLOW VISUALIZATION WITH PRESSURE MEASUREMENTS AT LOW SPEEDS ON THE NASA F-18 HIGH ALPHA RESEARCH VEHICLE (NASA) 45 p CSCL 01A
N90-28505
Unclas
G3/02 0305603

National Aeronautics and
Space Administration

ERRATA

NASA Technical Memorandum 101726

In-Flight Flow Visualization with Pressure Measurements at Low Speeds on the NASA F-18 High Alpha Research Vehicle

John H. Del Frate, David F. Fisher, and Fanny A. Zuniga

October 1990

Figure 18a (fuselage station 142) of NASA Technical Memorandum 101726 has been corrected. Please substitute page 8 in the text portion and page 32 in the graphics portion of this report with the enclosed corrections.

NASA Technical Memorandum 101726

In-Flight Flow Visualization with Pressure Measurements at Low Speeds on the NASA F-18 High Alpha Research Vehicle

John H. Del Frate, David F. Fisher, and Fanny A. Zuniga
NASA Ames Research Center, Dryden Flight Research Facility, Edwards, California

1990

National Aeronautics and
Space Administration
Ames Research Center
Dryden Flight Research Facility
Edwards, California 93523-0273

In-Flight Flow Visualization and Pressure Measurements at Low Speeds on the NASA F-18 High Alpha Research Vehicle

John H. Del Frate, David F. Fisher, and Fanny A. Zuniga

NASA Ames Research Center
Dryden Flight Research Facility
P.O. Box 273
Edwards, CA 93523-0273

1 ABSTRACT

In-flight results from surface and off-surface flow visualizations and from extensive pressure distributions document the vortical flow on the leading-edge extensions (LEXs) and forebody of the NASA F-18 high alpha research vehicle (HARV) for low speeds and angles of attack up to 50°. Surface flow visualization data, obtained using the emitted fluid technique, were used to define separation lines and laminar separation bubbles (LSB). Off-surface flow visualization data, obtained by smoke injection, were used to document both the path of the vortex cores and the location of vortex core breakdown. The location of vortex core breakdown correlated well with the loss of suction pressure on the LEX and with the flow visualization results from ground facilities. Surface flow separation lines on the LEX and forebody corresponded well with the end of pressure recovery under the vortical flows. Correlation of the pressures with wind-tunnel results show fair to good correlation.

2 INTRODUCTION

In recent years, more emphasis has been placed on expanding the envelope of fighter aircraft to include controlled flight at high angle of attack exceeding the maximum lift coefficient (C_L). Fighters such as the F-18 and F-16 use leading-edge extensions (LEXs) or wing body strakes which provide additional lift caused by the vortical flow these devices develop at moderate to high angles of attack (ref. 1). However, the prediction and control of this vortical flow and the mutual interactions of the vortices are not well understood. The combined effect of the LEX and the forebody vortices on the vehicle aerodynamics must be understood to avoid any adverse effects such as buffet or a loss of stability and control, and to take full advantage of the benefits that can be derived for fighter aircraft.

Vortical flow interactions on scale models in wind tunnels are not well understood at this time. Experimental data from different scale wind-tunnel F-18 models have shown conflicting results even when tested at the same Reynolds number (ref. 2). For example, the interaction of the forebody and LEX vortices on 6- and 7-percent scale F-18 models typically resulted in apparent lateral stability for all angles of attack, including stall and post stall regions. However, airplane flight data and wind-tunnel results for the large scale (16 percent) model at low Reynolds numbers indicated a region of lateral instability near maximum lift. This apparent scale effect is still being investigated. Understanding such scale effects is essential for successful design of future fighters intended to operate at high angles of attack.

NASA is currently conducting a High Alpha Technology Program (HATP) to (1) increase the understanding of the high angle of attack aerodynamics, (2) improve prediction techniques, (3) provide design guidelines, and (4) investigate new concepts for vortex control on advanced highly maneuverable aircraft.

This program uses the F-18 configuration as a validation and demonstration tool. The HATP incorporates wind-tunnel tests of subscale, (refs. 3 and 4), and full-scale models and components, calibration and validation information for computational fluid dynamics (CFD) codes, (refs. 5-9), piloted simulations and full-scale flight testing (refs. 10-17).

As part of this program, the Ames-Dryden Flight Research Facility has been conducting extensive flow visualization and pressure distribution studies on the NASA F-18 high alpha research vehicle (HARV) to document the characteristics of the forebody and the LEX vortices. Surface and off-surface flow visualization results have been reported in references 10 through 16. The off-surface flow visualization results presented were performed using smoke injection and are correlated to wind- and water-tunnel results. The surface flow visualization was performed using the emitted fluid technique. Pressure distribution results have been reported for the flight case in reference 16. The surface pressure measurements were made at five forebody stations and at three LEX stations on the aircraft and are correlated with similar data from a 6-percent wind-tunnel model and selected flow visualization data from flight.

This paper presents a selection of results from both the flow visualization and the pressure measurement studies conducted at low speeds and for angles of attack up to 50°.

3 NOMENCLATURE

b	aircraft span, ft
BART	Basic Aerodynamics Research Tunnel, NASA Langley Research Center
C_L	lift coefficient
C_p	pressure coefficient
C_p^*	pressure coefficient corresponding to local speed of sound, $C_p^* = \left(\frac{2}{\gamma M_\infty^2}\right)\left\{\left(\frac{(\gamma-1)M_\infty^2+2}{\gamma+1}\right)^{3.5} - 1\right\}$
d	diameter of fuselage forebody, in.
DTRC	David Taylor Research Center 7 × 10 transonic wind tunnel
ECM	electronic counter measures
F.S.	fuselage station, in. (nose apex at 59.82 in.)
FVF	Flow Visualization Facility water tunnel, NASA Ames-Dryden
HARV	high alpha research vehicle
HATP	High Alpha Technology Program
ℓ	length of aircraft from nose apex to engine exhaust plane, 54.4 ft
LEX	leading-edge extension
LSB	laminar separation bubble
LSWT	low-speed wind tunnel, McDonnell Aircraft Company
M_∞	free stream Mach number
m.a.c.	mean aerodynamic chord, 11.525 ft
R	reattachment line location
R_1	primary reattachment line location
R_2	secondary reattachment line location
R_3	tertiary reattachment line location
$Re_{\bar{c}}$	Reynolds number based on mean aerodynamic chord
Re_d	Reynolds number based on diameter
$Re_{d'}$	Reynolds number based on local maximum fuselage diameter, corrected for angle of attack using the method of reference 18.
s	local span distance from LEX-fuselage junction to LEX leading edge, in.
S_1	primary separation line location
S_2	secondary separation line location
S_3	tertiary separation line location
x	measured location along aircraft longitudinal axis, positive measured aft from nose, ft
Y	measured location along aircraft lateral axis, positive measured from center line out left wing, ft
y	distance along LEX local semispan, positive measured out left wing, in.
α	aircraft angle of attack, right wingtip angle-of-attack vane corrected for upwash and angular rates, deg
α'	angle of attack used in the determination of $Re_{d'}$, deg. At F.S. 70, 85, and 107, $\alpha' = \alpha$ - 5.6° because the nosecone is depressed from the aircraft waterline 5.6°. At F.S. 142 and 184, $\alpha' = \alpha$

β	aircraft angle of sideslip, average of left and right wingtip sideslip vanes corrected for angle of attack, positive nose left, deg
γ	ratio for specific heats of air, 1.4
θ	forebody cross section circumferential angle (0° is bottom centerline, positive is clockwise as seen from a front view, 0° to 360°), deg

4 VEHICLE DESCRIPTION

The NASA HARV (fig. 1) is a single-place preproduction F-18 aircraft built by McDonnell Douglas and Northrop and is powered by two General Electric F404-GE-400 afterburning turbofan engines. The aircraft features a mid-wing with leading- and trailing-edge flaps which operate on a schedule that is a function of angle of attack and Mach number. For $M_\infty \leq 0.76$ and $\alpha \geq 26°$, the leading-edge flap is down 33° (maximum) and the trailing-edge flap is at zero. The LEXs are mounted on each side of the fuselage from the wing roots to just forward of the canopy. The aircraft has twin vertical stabilizers canted out 20° from the vertical and differential all-moving horizontal tails. The NASA F-18 HARV, with the current flight control computers and control laws (8.3.3 programmed read only memory (PROM) set), is flown by NASA in the fighter escort configuration without stores. The aircraft carries no missiles and the wingtip missile launch racks have been replaced with special camera pods and wingtip airdata booms. The flight-test noseboom has been removed from the aircraft. The aircraft has an unrestricted angle-of-attack flight envelope in this configuration with the center of gravity between 17-percent and 25-percent mean aerodynamic chord (m.a.c.) as defined by the Naval Air Training and Operating Procedures Standardization (NATOPS) manual.

5 TEST TECHNIQUES, HARDWARE, AND INSTRUMENTATION

5.1 Off-Surface Flow Visualization Technique

The vortex cores were visualized using smoke as the tracer material as described in references 11 through 15 and similar to that described in reference 19. Smoke was introduced into the flow field through flush ports on the forebody at approximately 28 in. aft of the nose apex and circumferential angles (θs) of 80° and 280°. On the LEX, the smoke was routed to ducts which exhaust slightly below and approximately 4 in. aft of the LEX apex.

At the desired test conditions, the smoke was entrained in the flow field vortices which were videotaped and photographed with onboard cameras (fig. 1) or from chase aircraft (ref. 15). Smoke duration was normally 30 sec. The upper surfaces of the airplane were painted black to enhance visualization of the smoke traces.

5.2 Surface Flow Visualization Technique

The surface flow visualization technique used on the F-18 HARV consists of emitting liquid dye from flush orifices on the forebody and the LEX upper surface as shown in figure 2. These orifices, which were also used to gather pressure data, will be discussed in the next section. The hardware for the surface flow visualization system is described in detail in references 10 and 12 and is similar to that described in reference 20. The liquid dye used for this program consisted of a mixture of propylene glycol monomethyl ether (PGME) and a red toluene-based dye. The dye is emitted from orifices on the forebody and the LEX upper surface while the aircraft is at the desired flight condition. Upon evaporation of the solvents within the mixture, the dye is left on the surface of the aircraft and traces the surface flow streamlines as can be seen in figure 3. Photos are taken on the ground after the flight to document the surface flow streamlines.

5.3 Static Pressure Orifice Locations

Pressure measurements were made on both the forebody and the LEXs of the F-18 HARV (ref. 16) at fuselage locations selected to correspond with orifice locations on both the 0.06- and 0.16-scale wind-tunnel models (refs. 3 and 4).

Five rings of static pressure orifices were installed on the forebody forward of the canopy as shown in figure 2. At the first two rows, fuselage station (F.S.) 70 (x/ℓ = 0.015) and F.S. 85 (x/ℓ = 0.038), 32 static pressure orifices were spaced about the forebody. While at the last three rows, F.S. 107 (x/ℓ = 0.071), F.S. 142 (x/ℓ = 0.126) and F.S. 184 (x/ℓ = 0.190), 64 orifices were spaced about the forebody. For all the rows, the majority of the pressure orifices were placed on the upper surface where the greatest pressure gradients were expected.

Both the left and right LEXs were instrumented with three rows of pressure orifices located at F.S. 253 ($x/\ell = 0.295$), F.S. 296 ($x/\ell = 0.361$) and F.S. 357 ($x/\ell = 0.454$). The number of orifices installed at each station on the upper surface of each LEX varied from 13 to 20 and from 4 to 5 at each station on the lower surface.

Typical cross sections of the forebody and LEX orifice stations and the orientation of the orifices are given in figure 4. The view is looking aft on the aircraft with the bottom fuselage centerline at 0° and the top centerline fuselage at 180°. At the LEX stations, $y/s = 0.0$ is defined as the LEX fuselage junction while $y/s = 1.0$ is the leading edge of the LEX, $+1.0$ for the left LEX leading edge and -1.0 for the right LEX leading edge.

Several protrusions on the forebody should be noted. Two small, elliptical shaped electronic counter measures (ECM) antenna covers (fig. 4) were located on the sides of the fuselage centered at F.S. 134, $\theta = 85°$ and 275° and were approximately 9.5-in. long, 4-in. wide and protruded approximately 1.7 in. Also, two aircraft production pitot-static probes (fig. 4) were located on the lower fuselage at F.S. 164 to 177 and $\theta = 35°$ and 325°. The LEX was virtually free of significant protrusions forward of the orifice rows.

5.4 Airdata System

Airspeed, altitude, angle of attack (α), and angle of sideslip (β) were measured using airspeed booms shown in figure 5, mounted on specially designed wingtip photo pods as shown in figure 1. On the right wingtip a standard NACA noseboom (ref. 21), (fig. 5(a)), was installed with the tip mounted 7.3 ft forward of the wingtip leading edge. On the left wingtip, a swiveling probe (ref. 16), (fig. 5(b)), was similarly located. It is estimated that α and β were accurate to $\pm 0.5°$ for α up to 40°, and $\pm 1°$ for α up to 50°. It is also estimated that M_∞ is accurate to ± 0.005 at $\alpha = 50°$, and ± 0.003 for $\alpha < 30°$ (ref. 16).

6 FLIGHT-TEST PROCEDURES

The off-surface flow visualization data reported herein were obtained during 1-g flight conditions. The nominal altitudes were between 20,000 and 30,000 ft and the Mach numbers varied from approximately 0.2 to 0.4. Angles of attack ranged from 10° to approximately 54° over the course of this flight-test program, however, this report only presents results for $\alpha = 15.8°$ to 47.7°. Sideslip angles ranged from 7.5° to $-4.8°$ for the data in this report.

The on-surface flow visualization data were also obtained in 1-g stabilized flight. When the aircraft was at the desired angle of attack, the PGME dye was emitted through the flush orifices. The flight condition was held for approximately 75 sec to allow the PGME–dye mixture to set. One surface flow visualization test point was obtained for each flight with this method (ref. 10). Results are presented for $\alpha \sim 30°$ and 47°.

Surface pressure data presented were obtained in quasi-stabilized, 1-g flight maneuvers. Data were obtained at nominal altitudes of 20,000 and 45,000 ft. At the higher angles of attack, constant altitude could not be maintained during the 1-g maneuvers and data were obtained in a descent. Time segments of 0.4-sec duration were used for data analysis purposes. The data presented are for angles of attack from 10° to 50° with sideslip angle 0°.

A ground augmented guidance system similar to that described in reference 22 was implemented on the heads up display in the aircraft cockpit and used to assist the pilot to fly the desired flight conditions precisely.

7 RESULTS AND DISCUSSION

7.1 Description of F-18 Flow Field

The F-18's flow field is substantially dominated by vortices as seen in an example from a water-tunnel test shown in figure 6 at $\alpha = 30°$. The vortex cores noted on the figure are generated by flow which separates at moderate to high angles of attack from the forebody surface and at the sharp leading edge of each LEX. The LEX vortex cores are tightly wound and extend downstream until experiencing vortex core breakdown. Visible evidence of vortex core breakdown is a stagnation of flow in the core with a sudden expansion in the core diameter. Similarly, the forebody vortex cores extend downstream where they can interact with the LEX vortices. Interaction results in the forebody vortex cores being pulled beneath the LEX vortices and then redirected outboard.

8 EFFECT OF ANGLE OF ATTACK ON LEX VORTICES

8.1 Off-Surface Flow Visualization

The occurrence of vortex core breakdown has been reported to be particularly sensitive to an adverse pressure gradient along the vortex (ref. 23). It follows then that as angle of attack increases, thus moving the onset of the adverse pressure gradient forward, the vortex core breakdown location will move nearer the LEX apex. Examples of this trend are shown in figures 7(a–f). These wingtip still photos show the path of the LEX vortex core and its breakdown as photographed from the right wingtip camera at α = 15.8°, 20°, 24.2°, 29.9°, 35°, and 42.5° with approximately 0°-sideslip.

At α = 15.8°, (fig. 7(a)), the LEX vortex is already well developed with the core maintaining inboard and close to the surface extending over the LEX and breaking down aft of the wing trailing edge (not seen in photo). As the angle of attack increases from 20° to 35°, (figs. 7(b–e)), the LEX vortex breakdown, which was defined previously as the location where a stagnation of flow in the core occurs accompanied by a sudden expansion in the core diameter, moves forward from just in front of the vertical stabilizers to near the aft end of the canopy. At α = 42.5°, (fig. 7(f)), the vortex core was not observed and it is believed that the breakdown has moved all the way to very near the LEX apex.

The LEX vortex core breakdown location showed fore and aft fluctuations at steady-state flight conditions. Average longitudinal LEX vortex core breakdown locations were determined from onboard video cameras and are plotted as a function of angle of attack in figure 8. For angles of attack between 20° and 40°, the LEX vortex core breakdown position moved forward nearly linear with increasing angle of attack. On average, a 5°-change in angle of attack changes the longitudinal location 10 percent of the fuselage length.

The vortex core breakdown location was observed to fluctuate fore and aft more at longitudinal locations aft of $x/\ell = .43$. Due to the fore and aft fluctuations of the vortex core breakdown, the flight results are approximate to within $\pm .04\ x/\ell$.

In addition to the F-18 HARV flight results, figure 8 also includes results obtained with subscale models in water tunnel (ref. 15) and several wind-tunnel studies (refs. 4, 15). Even though there is a wide variation in model scale and Reynolds number and different fluid mediums, the plot shows reasonable agreement between data from the different sources.

8.2 Surface Flow Visualization

Presented in figures 9 and 10 are photographs of surface flow visualization on the LEX of the HARV using the emitted fluid technique for $\alpha \sim 30°$ and 47°, respectively. The fluid emitted from the orifices marks the surface streamlines. Where the streamlines merge, lines of separation are defined and conversely, where the streamlines diverge, lines of reattachment are defined. Observed in both figures 9 and 10, the secondary vortex line of separation (S_2) is defined by the inboard edge of the wide band of dye while the tertiary vortex line of separation (S_3) is defined by the outboard edge of the band. A schematic of the flow is shown in cross section in the inset of figure 9.

Although shown by the surface flow visualization technique, the secondary and tertiary vortices as shown in the schematic were not observed using smoke flow visualization. This was probably because of their relative weakness and small size as compared to the primary vortex and the location of the smoke injection.

In comparing the surface flow visualization data at $\alpha \sim 30°$ and 47°, the separation lines are observed to be farther outboard for the $\alpha \sim 47°$ case, especially at F.S. 357. As noted in the previous section, at $\alpha \sim 47°$, vortex core breakdown is very near the LEX apex. Even though vortex breakdown has already occurred, the secondary and tertiary lines of separation are still evident in the surface flow. While the flow appears highly unorganized, it is in fact structured, though extremely turbulent.

8.3 Measured Pressures

The effects of angle of attack on the LEX surface static pressure distribution are presented in figure 11 for angles of attack from 10° to 50° at the low speed ($0.2 < M_\infty < 0.4$), 1-g flight conditions. Pressure coefficients are plotted from the LEX as a function of LEX span, y and s as defined previously in figure 4. As the aircraft angle of attack increases from 10.0° to 25.8°, (figs. 11(a) and (b)), the LEX maximum suction pressure peaks increase in magnitude and move inboard. At F.S. 357, $\alpha \sim 30°$ and above (figs. 11(b) and (c)) the effect of the LEX vortex core breakdown on the pressure distribution can be seen. As shown in figure 8, at $\alpha = 30°$, vortex core breakdown occurs very near F.S. 357 ($x/\ell = 0.454$) and moves forward as angle of attack is increased further. This causes a decrease in the maximum suction pressure and a flattening of the pressure distributions when vortex core breakdown occurs at and moves forward of the measurement station. Similar trends are noted at F.S. 296 and F.S. 253 for $\alpha = 39.3°$ and 45.4°, respectively. At the highest angles of attack, (fig. 11(c)), the flow becomes less symmetrical, particularly at F.S. 253.

8.4 Correlation of LEX Pressure Distributions with Flow Visualization

Surface flow features from the surface flow visualization results previously presented in figures 9 and 10 for $\alpha \sim 30°$ and 47° have been correlated in figure 12 with the pressure distributions obtained on the LEX at $\alpha = 30.0°$ and 48.1°. Surface flow visualization was obtained only on the left LEX, however, the separation line locations are shown on both sides for comparison with the pressure distributions because they were obtained at near zero sideslip. At $\alpha \sim 30°$, (fig. 12(a)), the secondary separation lines, S_2, correspond well with the end of pressure recovery outboard of the maximum suction pressure peaks. The tertiary separation lines, S_3, seem to correspond with the end of pressure recovery inboard of the secondary suction peak near the LEX leading edge.

The lateral location of the primary vortex core on the F-18 HARV was determined with smoke visualization for $\alpha \sim 30°$ (refs. 15 and 16). The locations shown in figure 12(a) at F.S. 296 and 357 are just inboard of the maximum suctio pressure peaks. This agrees well with the lateral position of vortex cores on a sharp delta wing suggested by Hummel and Redeker in reference 24 and verified by Seshadri and Büetefisch in reference 25, which showed the lateral position of the vortex core coincided closely with the maximum suction peak.

At $\alpha = 48.1°$, (fig. 12(b)), the LEX primary vortex core breakdown occurred forward of F.S. 253 and all three stations experienced turbulent, buffeting vortical flow while the aircraft was in a mild wing rock. At F.S. 296 and 357 the pressure distributions were essentially flat and did not have distinct suction pressure peaks. At F.S. 253, the pressure distribution was slightly asymmetrical and the end of pressure recovery did not correspond as well with the separation lines caused in part by the unsteadiness of the flow and the difficulty in locating the separation lines at this condition.

8.5 Correlation of Flight and Wind-Tunnel Pressure Distributions on LEX

The LEX pressure distribution results from a 6-percent scale F-18 model (ref. 4) are correlated with flight data at $\alpha \sim 30°$ at $M_\infty \sim 0.3$ and at $\alpha = 50°$ at $M_\infty \sim 0.2$ in figure 13. Wind-tunnel data was available from only the upper surface of the LEX. At $\alpha \sim 30°$, (fig. 13(a)), the wind tunnel tends to underpredict slightly the suction pressures at F.S. 253 and 296. The suction pressure peaks are predicted better at F.S. 357. Both the flight and wind-tunnel results indicate some asymmetry in the LEX pressure distributions at $\alpha = 50°$, (fig. 13(b)).

9 EFFECT OF ANGLE OF ATTACK ON FOREBODY VORTICES

9.1 Off-Surface Flow Visualization

Two photographs of smoke entrained in the right forebody vortex core, taken from the right wingtip camera, are shown in figures 14(a and b) for $\alpha = 29.5°$ and 47.7°, and $\beta \sim 0°$. At both angles of attack, the right forebody vortex core is well defined. At 29.5°, (fig. 14(a)), the forebody vortex stays very close to the aircraft surface as it moves over the top of the canopy and aft over the fuselage. In contrast, the forebody vortex core at $\alpha = 47.7°$, (fig. 14(b)), lies farther away from the surface of the aircraft from its point of origin and continues to a location aft of the canopy where it appears to be drawn down into the region directly above the LEX. Additionally, the forebody vortex core at 47.7° appears to have a larger diameter.

The forebody vortices do not appear to be as strong as the LEX vortices because of the lack of persistence and uniformity in the core definition. In fact, over the course of the 100-flight series, natural flow visualization of the forebody vortices caused by condensation was observed by the pilot only once whereas the LEX vortices were observed frequently.

9.2 Surface Flow Visualization

Surface flow visualization on the forebody of the HARV using the emitted fluid technique is presented in the photos of figures 15 and 16 for $\alpha \sim 30°$ and 47°, respectively. Noted in the figures are the primary vortex separation lines (S_1), secondary separation lines (S_2), the lines of reattachment (R), and the laminar separation bubbles (LSBs). A cross section view of the flow about the forebody is shown in the inset (fig. 15). Again, the separation and reattachment lines are defined as they were for the LEX. An LSB was observed on the forebody, appearing as a kink in the surface flow streamlines. This is confirmed by noting that this only occurred near the nose apex and that at $\alpha \sim 47°$, (fig. 16(b)), the turbulent boundary layer from the screwheads shown on the forebody do not create a kink in the surface streamlines.

A comparison of the forebody surface flow visualization at $\alpha \sim 30°$ with that obtained at 47° shows that the separation lines at $\alpha \sim 47°$ have moved much nearer the nose apex. This indicates a stronger, more fully developed vortex system at $\alpha \sim 47°$. In both cases, the separation lines appear to be nearly symmetrical for $\beta \sim 0°$.

9.3 Measured Pressures

The effects of angle of attack on the forebody pressure distribution are presented in figure 17 for angles of attack from 10° to 50° at low speed, 1-g flight conditions. Pressure coefficients are presented as a function of circumferential angle, θ, and for each of the five forebody stations. Note the change in scale from the LEX results. The maximum suction pressures are much greater in magnitude for the LEX (fig. 11) than for the forebody at the same angle of attack (fig. 17).

At F.S. 70, F.S. 85 and F.S. 107, and starting at $\alpha = 19.7°$, (fig. 17(a)), the flow accelerating around the forebody induces a pair of maximum suction pressure peaks on the sides of the fuselage at $\theta \sim 100°$ to 120° and 240° to 260°. As the angle of attack was increased, these maximum suction peaks became much more pronounced, (figs. 17(b) and (c)). At F.S. 85 and 107, the forebody primary vortex pair footprints (ref. 4), indicated by suction pressure peaks at $\theta = 168°$ and 192°, first become evident at $\alpha = 34.3°$ (fig. 17(b)). As the angle of attack is increased, these footprints become more negative and indicate the presence of the primary vortex cores above the surface (ref. 26). It should be noted that at these fuselage stations the pressure distributions in all cases are symmetrical about $\theta = 180°$ for $\beta \sim 0$ for angles of attack up to 50°.

At F.S. 142, sharp peaks at $\theta = 90°$ and 270° in the pressure coefficient curve starting at $\alpha = 19.7°$ (fig. 17(a)), are the result of local separation behind the two small, elliptical shaped ECM antenna covers described previously under Experiment Description. As the angle of attack is increased to 50° (fig. 17(c)), these peaks move up around the fuselage to $\theta = 108°$ and 252°.

At F.S. 142, the forebody cross section has become elliptical in shape. The magnitude of the maximum suction pressure peaks at this location have become somewhat diminished above $\alpha \sim 25°$ or 30°, (figs. 17(b) and (c)), compared to the three forward stations. Distinct footprints of the primary vortex are present near $\theta \sim 160°$ and 200° beginning around $\alpha = 25°$ (fig. 17(b)). These footprint peaks are less distinct at $\theta \sim 160°$ than at $\theta \sim 200°$ because this area of the aircraft contains the doors for the in-flight refueling probe and is not as smooth and flush as the left side where there are no doors, joints, or other discontinuities. These footprints have a maximum magnitude at $\alpha = 45°$ diminishing significantly at $\alpha = 50°$, probably indicating that the vortices have begun to lift from the surface. Again, the pressure distributions are generally symmetrical about $\theta = 180°$ with the differences accounted for by local protuberances or discontinuities.

At F.S. 184, the maximum suction pressure peaks have moved up to $\theta \sim 120°$ and 240°, (figs. 17(b) and (c)), caused by the local influence of the LEX. At this station, the apex of the LEXs is only 13 in. aft, (fig. 4), and is located at $\theta \sim 123°$ and 237°. As can be seen in figure 4, the surface flow visualization shows the streamlines pulled up and over the LEX for $\alpha \sim 26°$. The maximum suction peaks for $\alpha > 25°$ are further reduced in magnitude compared to F.S. 142 because the primary vortices are lifted farther from the surface. The primary vortex footprints at $\theta \sim 165°$ and 195° can still be observed at $\alpha > 25°$, (figs. 17(b) and (c)), but are more diminished in magnitude compared to those at F.S. 142. For $\alpha = 34.3°$ and greater, the peaks in the pressure coefficient curves at $\theta \sim 48°$ to 60° and 300° to 312° are due to local separation caused by the aircraft production pitot-static probes mentioned previously. Again, at this location, the pressure distributions are nearly symmetrical about θ = 180° with only small differences in the primary vortex footprint due to discontinuities caused by the refueling probe doors.

The general trend in the data from the forebody is for the maximum suction pressure peaks to first appear at $\alpha \sim 20°$ and increase in magnitude as angle of attack is increased. In addition, the footprints of the primary vortex first appear at $\alpha \sim 25°$ at F.S. 142 and F.S. 184 and progress forward toward the nose apex as the angle of attack is increased.

9.4 Correlation of Forebody Pressure and Flow Visualization Results

Surface flow visualization results for $\alpha \sim 30°$ and 47° (figs. 15 and 16) are correlated with forebody flight pressure distributions at $\alpha = 30.0°$ and 48.1° in figure 18. The surface flow visualization and the forebody pressure measurements were obtained on separate flights. Some differences in the results can therefore be expected because of slightly different test conditions and test techniques.

In figure 18(a) at F.S. 70 and for $\alpha \sim 30°$, and in figure 18(b) at F.S. 70, F.S. 85, and F.S. 107 and for $\alpha \sim$ 47°, LSBs were identified in the surface flow visualization (ref. 13). Laminar separation bubbles are more closely identified with the critical Reynolds number range ($2 \times 10^5 < Re_d < 4 \times 10^5$) than the supercritical range ($4 \times 10^5 < Re_d < 6 \times 10^6$) (ref. 24). The $Re_{d'}$ values for the flight data are given in the figures. At F.S. 107, (fig. 18(b)), the LSB located by the surface flow visualization at θ = 113° and 247° correlates well with the kinks in the pressure distribution at θ = 108° to 114° and 246° to 252°. This is consistent with the discussion in reference 27 where the kink or flattening in the pressure distribution was correlated with an LSB for a tangent-ogive cylinder. Laminar separation kinks in the pressure distribution are also noted for the data at α = 30° at F.S. 107, (fig. 18(a)), though laminar separation was only noted in the surface flow visualization near F.S. 70. Unfortunately, the orifices were not dense enough to define the kinks in the pressure distribution caused by the LSB at F.S. 70 and F.S. 85. The kinks on the windward side of the maximum suction pressure peaks at F.S. 107 for θ = 84° to 90° and 270° to 276° are not explained at this time. No deviation in the surface streamlines was detected in the flow visualization at these circumferential locations.

The peaks in the pressure distributions for F.S. 142 at $\theta \sim 95°$ and 265°, (fig. 18(a)), are caused by the ECM antenna covers as noted earlier.

The primary separation lines, S_1, as identified by the surface flow visualization in figures 15 and 16, correlated well with the end of pressure recovery on the lee side of the forebody. This can be seen most clearly in figure 18(b) at F.S. 85 to 184 and in figure 18(a) at F.S. 142 and 184. This correlation also agrees well with the data of references 26 and 27 for a cone and an ogive. Also shown in figure 18, the secondary vortex separation line, S_2, occurs slightly outboard of the footprints of the primary vortex pairs at F.S. 142 and F.S. 184 in figure 18(a) and at F.S. 107 to 184 in figure 18(b).

9.5 Correlation of Flight and Wind-Tunnel Pressure Distributions on Forebody

Forebody pressure distribution results from a 6-percent scale F-18 model (ref. 4) are correlated with flight data at $\alpha \sim 30°$ at $M_\infty \sim 0.3$ and at $\alpha = 50°$ at $M_\infty \sim 0.2$ in figure 19. Wind-tunnel data were available at only three forebody fuselage stations, F.S. 107, 142, and 184.

In figure 19(a), flight and wind-tunnel data are presented for $\alpha = 30.0°$ and $M_\infty \sim 0.3$. At these conditions, the comparisons are good with the exception at F.S. 142 where the wind-tunnel data does not indicate the footprints of the primary vortex pair at $\theta \sim 160°$ and 200°. The wind-tunnel model did not simulate the protuberances caused by the ECM antenna covers, the production probes, and the refueling doors and hence, these effects are not present. At F.S. 107, there appears to be a kink in the wind-tunnel pressure distribution caused by an LSB at $\theta \sim 120°$ to 132°, which is slightly more leeward than the flight values. The model and flight Reynolds numbers, $Re_{d'}$, for all three stations are all in the supercritical range though the flight values are almost an order of magnitude greater.

Results from flight and wind-tunnel data at $\alpha = 50.0°$ and $M_\infty \sim 0.2$ are presented in figure 19(b). At these conditions, the comparison of the results is mixed. The model Reynolds numbers, $Re_{d'}$, in this case are critical whereas the flight values are supercritical. The footprints of the primary vortex are evident for both the flight and wind-tunnel data. At F.S. 107, the wind-tunnel maximum suction pressure coefficients are approximately 0.2 lower in magnitude than the flight values, however the location of the LSBs and the pressure distributions at the primary vortex footprints agree well. At F.S. 142 the data at the maximum suction pressure peaks compare well but the comparison is not as good at the primary vortex footprints. At F.S. 184, there appears to be an asymmetry in the wind-tunnel pressure distribution that does not appear in the flight data.

10 FOREBODY–LEX VORTEX ASYMMETRIES AND INTERACTIONS

The effects of angle of attack on the LEX and forebody flows have been shown in the previous sections using both off-surface and surface flow visualization techniques as well as surface pressure measurements. In this section, the effect of sideslip and the forebody–LEX vortex interactions will be discussed using only the off-surface flow visualization technique.

10.1 Effect of Sideslip on LEX Vortices

The effect of angle of sideslip on the vortex core breakdown position is illustrated in figures 20(a–c) as photographed from the right wingtip camera during a wings level sideslip maneuver at $\alpha \sim 25°$. The right LEX vortex core breakdown position can be seen moving aft as sideslip angle is decreased from 4.5° (right LEX vortex on windward side) to −3.4° (right LEX vortex on leeward side) where positive angle of sideslip is flow from the right or nose left as viewed by the pilot.

The following trends were observed from studying the onboard video data as well as from the wingtip still photos. With sideslip, the windward vortex core moves inboard and down closer to the surface with breakdown occurring much farther forward than at 0° sideslip. Conversely, the leeward vortex core was observed to move outboard and away from the surface with the vortex core breaking down farther aft than at 0° sideslip.

The breakdown location was determined using onboard video data, and plotted in figure 21 for $\alpha \sim 20°$, 25°, and 30°. In this figure, the lateral location of the vortex core breakdown was plotted against longitudinal location of the vortex core breakdown for positive, negative, and 0°-sideslip conditions.

Figure 21 shows that at $\alpha \sim 20°$, for the small sideslip angles of this study, the vortex breakdown moves more along the longitudinal direction than in the lateral direction, however, this effect is reduced as angle of attack increases.

10.2 Forebody–LEX Vortex Interactions

10.2.1 Angle of Attack Effects

Shown in figures 22(a–c) is a series of photos of the right forebody vortex taken with the right wingtip camera for α = 29.5° to 42.5° at $\sim$ 0°-sideslip. In the photos it can be observed that an interaction between the forebody and LEX vortex cores exists (inset sketches which have been reconstructed from other flight data are shown for clarity). At α = 29.5° (fig. 22(a)), the forebody vortex core is pulled down beneath the LEX vortex just aft of the LEX/wing leading-edge flap hinge junction. As the angle of attack increases, (figs. 22(b–c)), the location of this interaction moves forward. The longitudinal location of this interaction is plotted in figure 23 as a function of angle of attack. Accuracy of the data is $x/\ell = \pm.04$.

Also plotted in figure 23 is the location of the LEX vortex core breakdown taken from figure 8. It should be noted that the forebody–LEX vortex interaction, for the presented αs in 0°-sideslip cases, occurs aft of the LEX vortex core breakdown position. Since the diameter of the LEX vortex structure increases significantly after breakdown as seen previously from wingtip photographs, it is not surprising that the forebody vortex core might be pulled under the LEX vortex core because of the downward action of the LEX vortex which is now closer to it because of its suddenly increased diameter.

The forebody–LEX interaction locations gathered from a water-tunnel test on a 3-percent scale F-18 model (ref. 15) are also plotted on figure 23. Good correlation between the flight and the model data is found in spite of a large difference in Reynolds number and fluid medium.

10.2.2 Sideslip Effects

Sideslip has a significant effect on the forebody vortices. Forward of the canopy, the two forebody vortices are nearly symmetrical at $\beta \sim 0°$, for the angles of attack presented. With sideslip, these vortices are rotated about the forebody to an asymmetrical location similar to the schematic of figure 24. The rotation of the forebody vortices due to sideslip was also illustrated in a report by Erickson (ref. 12) where F/A-18 water-tunnel flow visualization photos showed the leeward primary separation line rotated down and that of the windward side rotated up.

At the higher angles of attack, the effect of sideslip causes the windward forebody vortex to travel up and over the top of the canopy. In some cases, this windward forebody vortex core has been observed to cross the aircraft centerline and interact with the leeward LEX vortex near the vertical tails. At the same time, the leeward forebody vortex moves along the side of the canopy to interact and merge with the leeward LEX vortex near the canopy. The location of this forebody–LEX interaction as determined from onboard video and still photos is shown in figure 25 as a function of sideslip for an $\alpha \sim 33°$.

From figure 25 it can be seen that as the aircraft experiences greater sideslip angles, the interaction of the leeward forebody vortex core with the LEX vortex core occurs farther forward, and the windward forebody vortex core does so farther aft. This appears to be caused by the location of the forebody vortices as affected by angle of sideslip. With sideslip, the windward forebody vortex is moved up and over toward the top of the canopy and away from the corresponding LEX vortex. Conversely, at the same time, the leeward forebody vortex is moved down along the side of the canopy and closer to the corresponding LEX vortex.

Upon comparing the effect of sideslip on the longitudinal movement of the forebody–LEX vortex core interaction and the longitudinal movement of the LEX vortex cores, it was noted that the trends opposed each other. As sideslip increased, the breakdown location of the windward LEX vortex core moved forward while the location of the windward forebody–LEX vortex interaction moved aft. The inverse was true on the leeward side.

11 CONCLUDING REMARKS

A low-speed correlation of in-flight flow visualization, surface pressure measurements, water-tunnel, and wind-tunnel results for the vortical flows on the forebody and leading-edge extensions of an F-18 aircraft have been reported for angles of attack up to 50°. Both off-surface flow visualization using smoke injection and surface flow visualization using the emitted liquid dye technique were used to obtain photographic data from flight. In-flight surface pressure measurements were made at five forebody stations and at three LEX stations on the aircraft and were correlated with similar data from a 6-percent scale wind-tunnel model.

The off-surface flow visualization showed a strong vortical field above the LEX and that the LEX vortex core breakdown location moved forward with increasing angle of attack. The LEX vortex core breakdown from wind-tunnel and water-tunnel tests correlated reasonably well with the flight results. In general, as angle of attack increased, the LEX pressure distributions experienced an increase in the magnitude of the maximum suction pressure peaks as the vortex core breakdown approached them and then a decrease and the general flattening of the pressure distribution as the vortex core breakdown progressed forward of them. The LEX secondary separation, as determined from surface flow visualization, corresponded well with the end of pressure recovery outboard of the maximum suction pressure peaks. The wind-tunnel data tended to underpredict the suction pressures at some locations at $\alpha = 30°$. Both flight and wind-tunnel results showed asymmetries at $\alpha = 50°$.

Vortical flow was also observed on the forebody using flow visualization starting at $\alpha \sim 25°$. The general trend for the forebody pressure distributions was for the maximum suction pressure peaks to first appear at $\alpha \sim 19°$ and increase in magnitude as the angle of attack was increased. Footprints of the primary vortex pairs first appeared at $\alpha \sim 25°$ on the aft portion of the forebody and progressed forward as the angle of attack increased. The forebody primary separation lines, as identified by surface flow visualization, correlated well with the end of pressure recovery leeward of the maximum suction peak. Both the surface pressure C_p levels and the off-surface flow visualization indicated that the forebody vortex system is weaker than the LEX vortex system. At $\alpha = 30°$, the comparison of the flight and wind-tunnel pressure distributions were in general, good, but the wind-tunnel data did not show the presence of the vortex footprints and also exhibited some asymmetry not present in the flight data.

Interactions were observed between the forebody and LEX vortical flow fields. These interactions were both a function of angle of attack and sideslip. The effect of angle of sideslip was to cause asymmetrical forebody–LEX interactions as well as asymmetrical LEX vortex core breakdown.

12 REFERENCES

1. Skow, A.M., G.E. Erickson, "Modern Fighter Aircraft Design for High-Angle-of-Attack Maneuvering," AGARD LS-121, Paper No. 4, 1982.
2. Erickson, Gary E., *Water Tunnel Flow Visualization and Wind Tunnel Data Analysis of the F/A-18*, NASA CR-165859, 1982.
3. Banks, Daniel W., "Wind-Tunnel Investigation of the Forebody Aerodynamics of a Vortex-Lift Fighter Configuration at High Angles of Attack," SAE Paper 881419, Oct. 1988.
4. Erickson, G.E., R.M. Hall, D.W. Banks, J.H. Del Frate, J.A. Schreiner, R.J. Hanley, and C.T. Pulley, "Experimental Investigation of the F/A-18 Vortex Flows at Subsonic Through Transonic Speeds, Invited Paper," AIAA 89-2222, 1989.
5. Thomas, James L., Robert W. Walters, Taekyu Reu, Farhad Ghaffari, Robert P. Weston, and James M. Luckring, "A Patched-Grid Algorithm for Complex Configurations Directed Toward the F/A-18 Aircraft," AIAA 89-0121, Jan. 1989.
6. Ghaffari, F., J.M. Luckring, J.L. Thomas, and B.L. Bates, "Navier-Stokes Solutions about the F/A-18 Forebody-LEX Configuration," AIAA 89-0338, Jan. 1989.
7. Schiff, Lewis B., Russell M. Cummings, Reese L. Sorenson, and Yehia M. Rizk, "Numerical Simulation of High-Incidence Flow over the F-18 Fuselage Forebody," AIAA 89-0339, Jan. 1989.
8. Schiff, Lewis B., Russell M. Cummings, Reese L. Sorenson, and Yehia M. Rizk, *Numerical Simulation of F-18 Fuselage Forebody Flow at High Angles of Attack*, NASA CP-10038, vol. 1, 1989, pp. 345-359.
9. Cummings, Russell M., Yehia M. Rizk, Lewis B. Schiff, and Neal M. Chaderjian, "Navier-Stokes Predictions of the Flowfield Around the F-18 (HARV) Wing and Fuselage at Large Incidence," AIAA 90-0099, Jan. 1990.
10. Fisher, David F., David M. Richwine, and Daniel W. Banks, *Surface Flow Visualization of Separated Flows on the Forebody of an F-18 Aircraft and Wind-Tunnel Model*, NASA TM-100436, 1988. Also AIAA 88-2112.
11. Curry, Robert E., and David M. Richwine, "An Airborne System for Vortex Flow Visualization on the F-18 High-Alpha Research Vehicle," AIAA 88-4671, Sept. 1988.
12. Fisher, David F., and Robert R. Meyer, Jr., *Flow Visualization Techniques for Flight Research*, NASA TM-100455, 1988. Also in "Flight Test Techniques," AGARD CP 452, paper no. 20.
13. Fisher, David F., John H. Del Frate, and David M. Richwine, "In-Flight Flow Visualization Characteristics of the NASA F-18 High Alpha Research Vehicle at High Angles of Attack," SAE Paper 892222, Sept. 1989.
14. Schneider, Edward T., and Robert R. Meyer, Jr., "F-18 High Alpha Research Vehicle: Description, Results and Plans," SETP 33rd Symposium Proceedings, Sept. 1989.
15. Del Frate, John H. and Fanny A. Zuniga, "In-Flight Flow Field Analysis on the NASA F-18 High Alpha Research Vehicle With Comparisons to Ground Facility Data," AIAA 90-0231, Jan. 1990.
16. Fisher, David F., Daniel W. Banks, and David M. Richwine, "F-18 High Alpha Research Vehicle Surface Pressures: Initial In-Flight Results and Correlation with Flow Visualization and Wind-Tunnel Data," AIAA 90-3018, Aug. 1990.
17. Whitmore, Stephen A., Timothy R. Moes, and Terry J. Larson, *Preliminary Results From a Subsonic High Angle-of-Attack Flush Airdata Sensing (HI-FADS) System: Design, Calibration, and Flight Test Evaluation*, NASA TM-101713, 1990.
18. Polhamus, Edward C., *A Review of Some Reynolds Number Effects Related to Bodies at High Angles of Attack*, NASA CR-3809, 1984.

19. Fennell, L.J., "Vortex Breakdown—Some Observations in Flight on the HP115 Aircraft," Reports and Memoranda No. 3805, Sept. 1971. (Replaces R.A.E. Technical Report 71177 - A.R.C. 34 400).

20. Bisgood, P.L., "The Application of a Surface Flow-Visualisation Technique in Flight," Reports and Memoranda No. 3769, Feb. 1974. (Replaces R.A.E. Technical Report 74022 - A.R.C. 35 554).

21. Richardson, Norman R., and Albin O. Pearson, *Wind-Tunnel Calibrations of a Combined Pitot-Static Tube, Vane-Type Flow-Direction Transmitter, and Stagnation-Temperature Element at Mach Numbers From 0.60 to 2.87*, NASA TN D-122, 1959.

22. Meyer, Robert R., Jr., and Cdr. Edward T. Schneider, *Real-Time Pilot Guidance System for Improved Flight Test Maneuvers*, AIAA 83-2747, Nov. 1983. See also NASA TM-84922, 1984.

23. Payne, Francis M., "The Structure of Leading Edge Vortex Flows Including Vortex Breakdown," A Dissertation from the Aerodynamics Laboratory, Department of Aerospace and Mechanical Engineering, University of Notre Dame, IN, May 1987.

24. Hummel, D. and G. Redeker, *Experimental Determination of Bound Vortex Lines and Flow in the Vicinity of the Trailing Edge of a Slender Delta Wing*, NASA Technical Translation, NASA TT F-15,012, 1973.

25. Seshadri, S.N. and Karl-Aloys Büetefisch, "Evaluation of LDA 3-Component Velocity Data on a 65° Delta Wing at M = 0.85 and First Results of an Analysis," DFVLR-FB 89-19, 1989.

26. Peake, D.J., D.F. Fisher, and D.S. McRae, "Flight, Wind Tunnel, and Numerical Experiments with a Slender Cone at Incidence," AIAA Journal, Vol 20, No. 10, p. 1338, Oct. 1982.

27. Hall, Robert M., "Influence of Reynolds Number on Forebody Side Forces for 3.5-Diameter Tangent-Ogive Bodies," AIAA 87-2274, Aug. 1987.

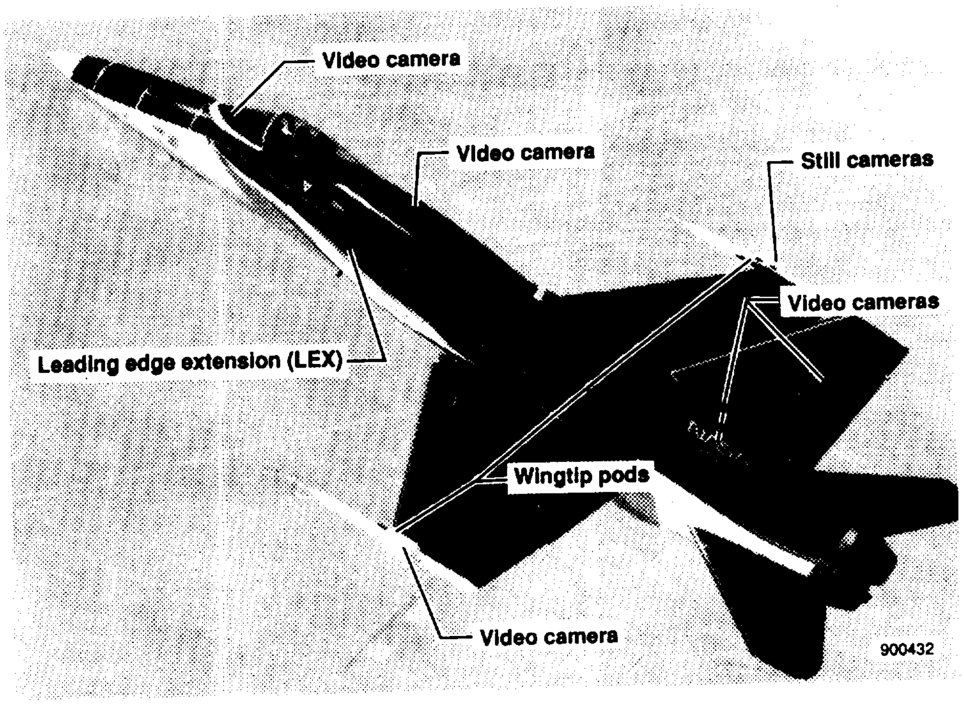

Figure 1. The F-18 HARV.

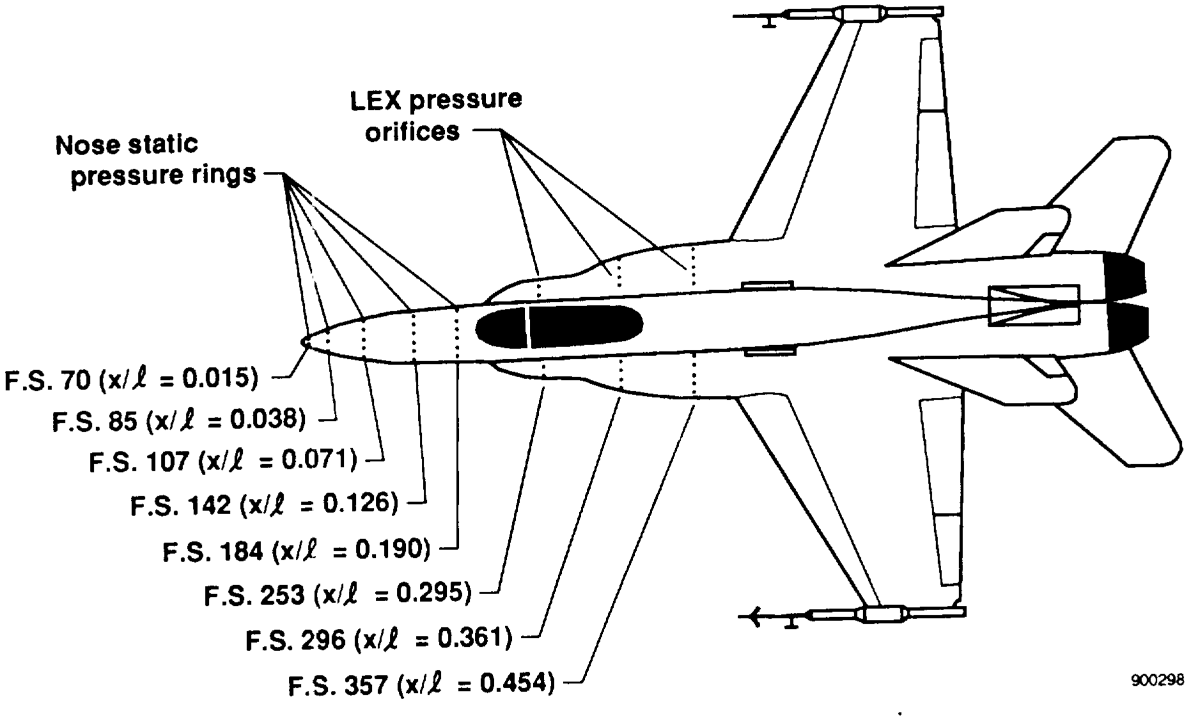

Figure 2. Forebody and LEX pressure measurement stations.

ORIGINAL PAGE
BLACK AND WHITE PHOTOGRAPH

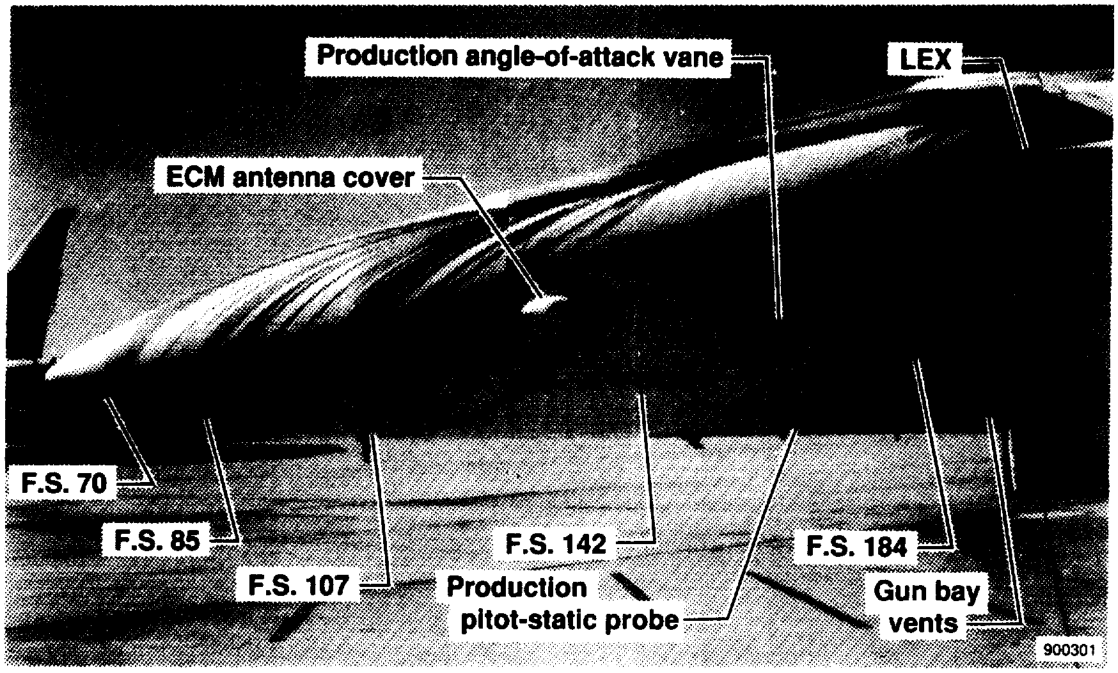

Figure 3. Locations of protrusions near forebody pressure measurement stations. Surface flow streamlines marked using emitted fluid techniques (shown for $\alpha = 26°$).

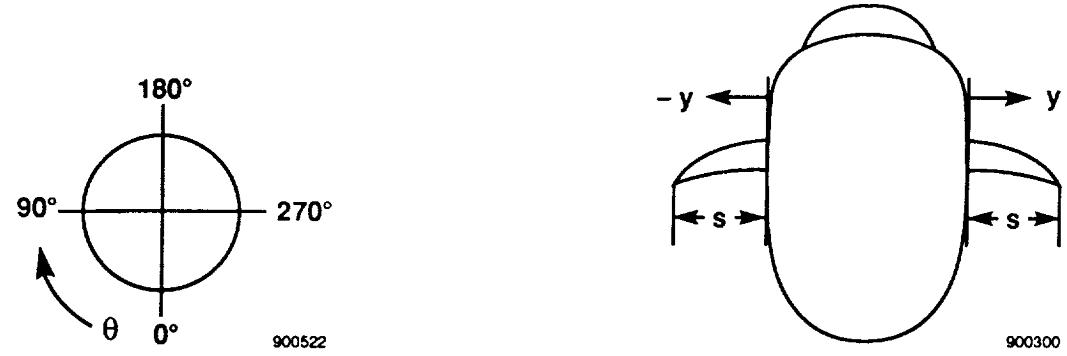

(a) Forebody circumferential angle.

(b) LEX spanwise position.

Figure 4. Typical cross sections of pressure measurement stations and orifice orientation, looking aft.

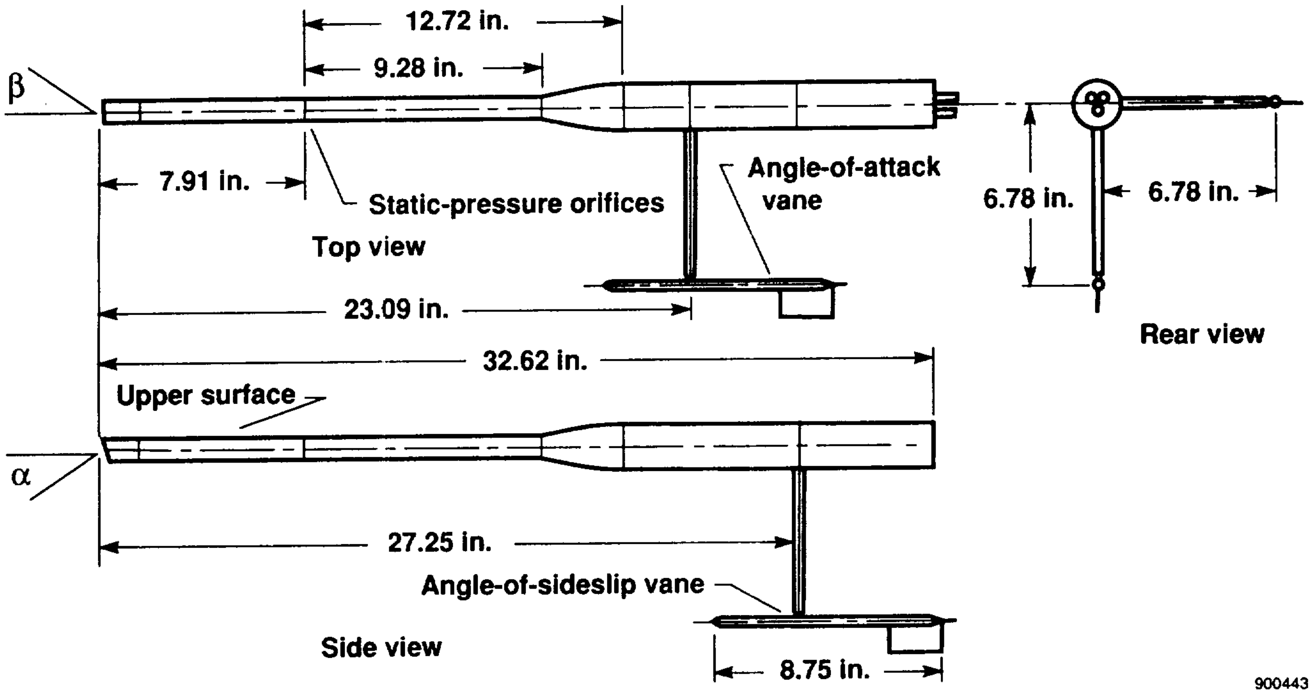

(a) NACA airdata probe, right wingtip, (ref. 21).

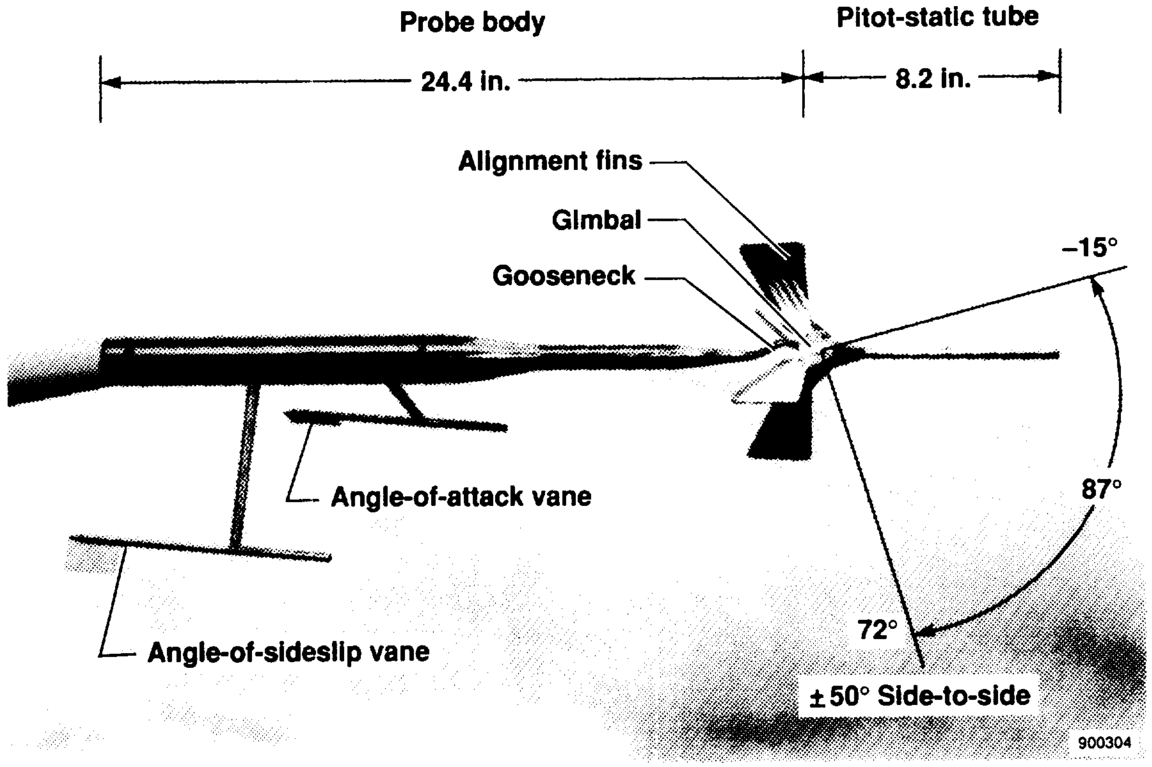

(b) Swiveling-head airdata probe, left wingtip.

Figure 5. Airdata probes mounted on F-18 HARV wingtips.

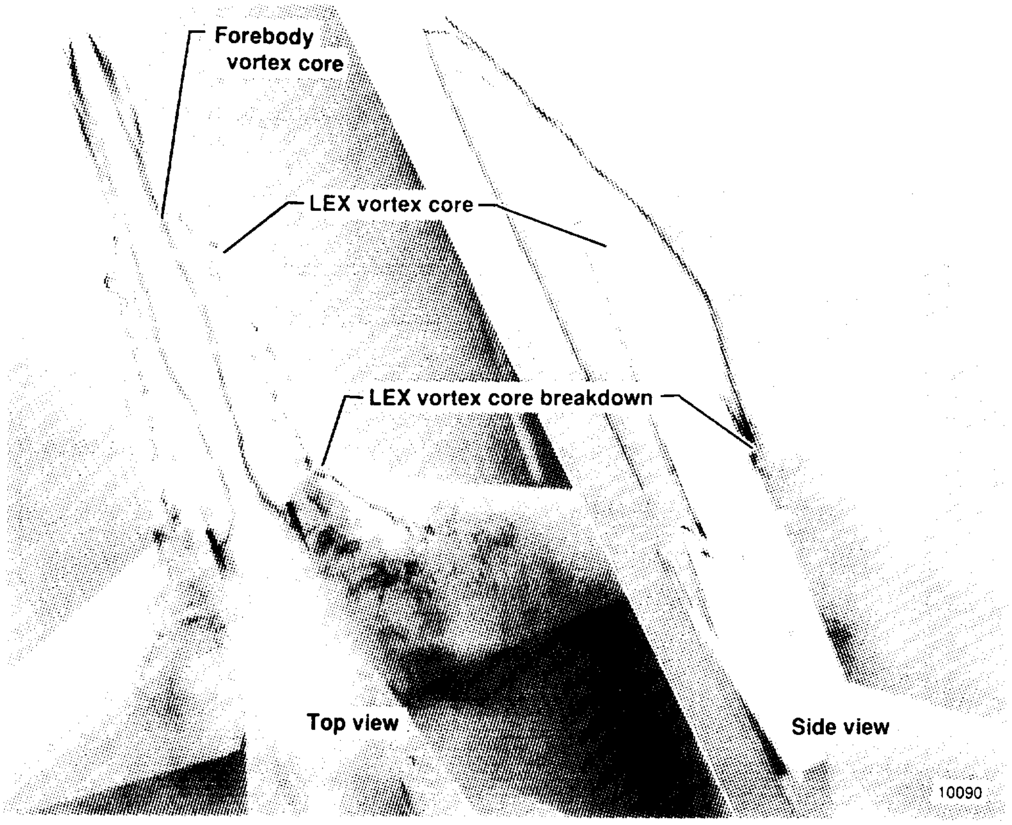

Figure 6. Vortex flow on a 3-percent model of the F-18 airplane in a water tunnel, $\alpha = 30°$, $\beta = 0°$, (ref. 15).

ORIGINAL PAGE
BLACK AND WHITE PHOTOGRAPH

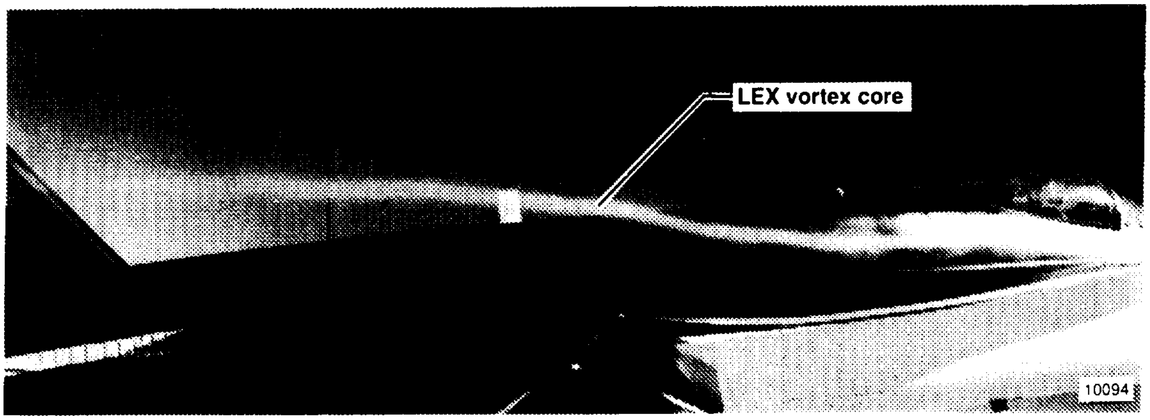

(a) $\alpha = 15.8°$ and $\beta = 0.2°$.

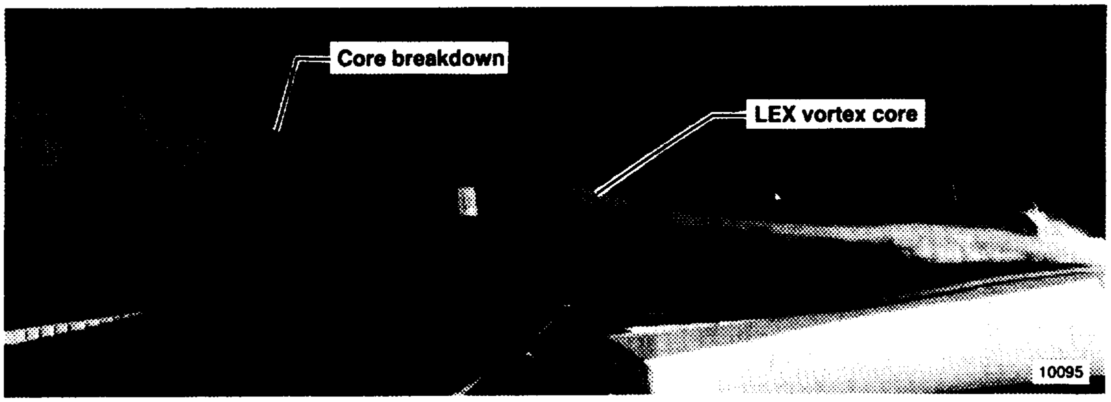

(b) $\alpha = 20°$ and $\beta = 0°$.

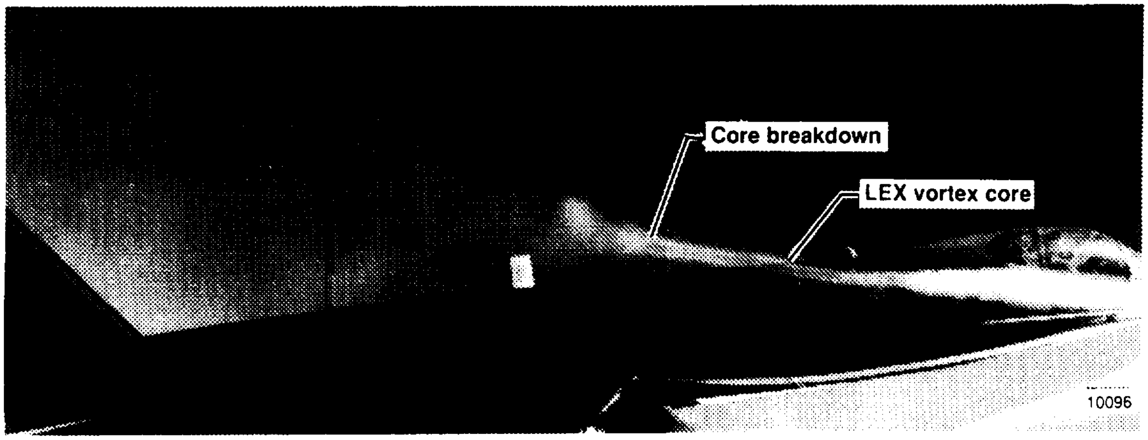

(c) $\alpha = 24.2°$ and $\beta = -0.8°$.

Figure 7. Right wingtip view showing effects of increased angle of attack on LEX vortex core and breakdown point.

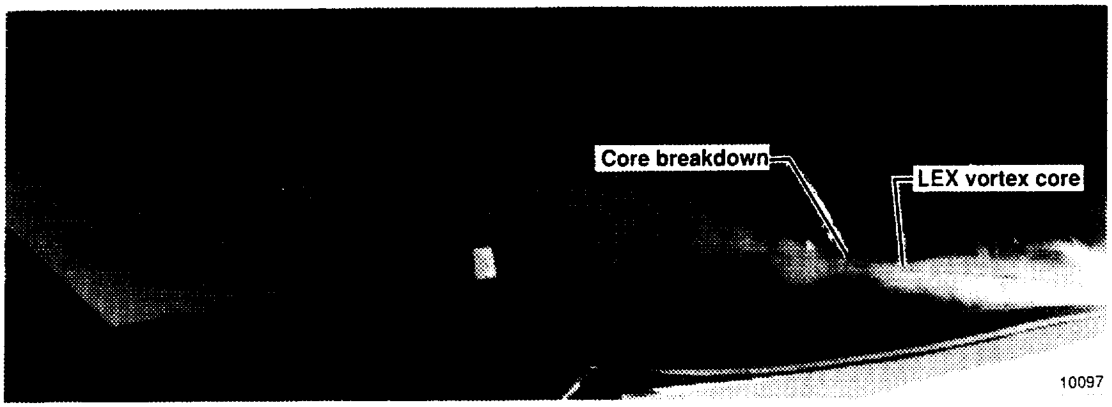

(d) $\alpha = 29.9°$ and $\beta = 0.3°$.

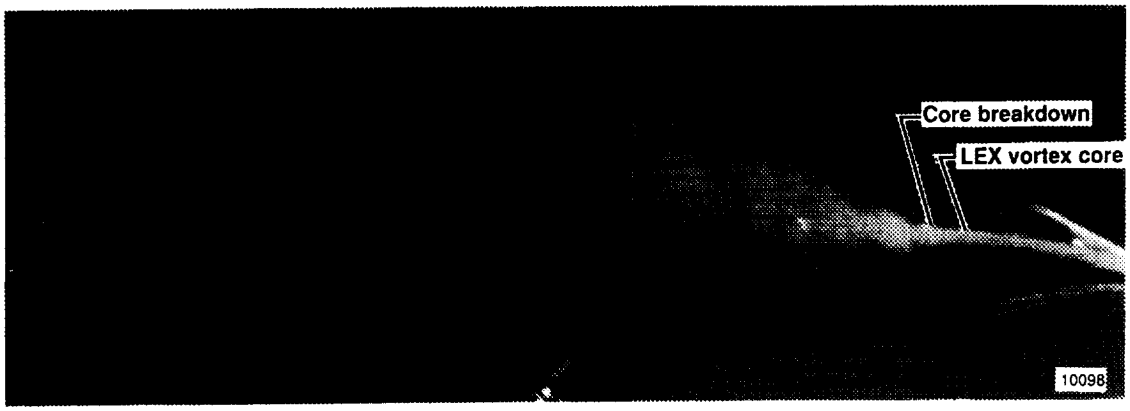

(e) $\alpha = 35°$ and $\beta = 1.8°$.

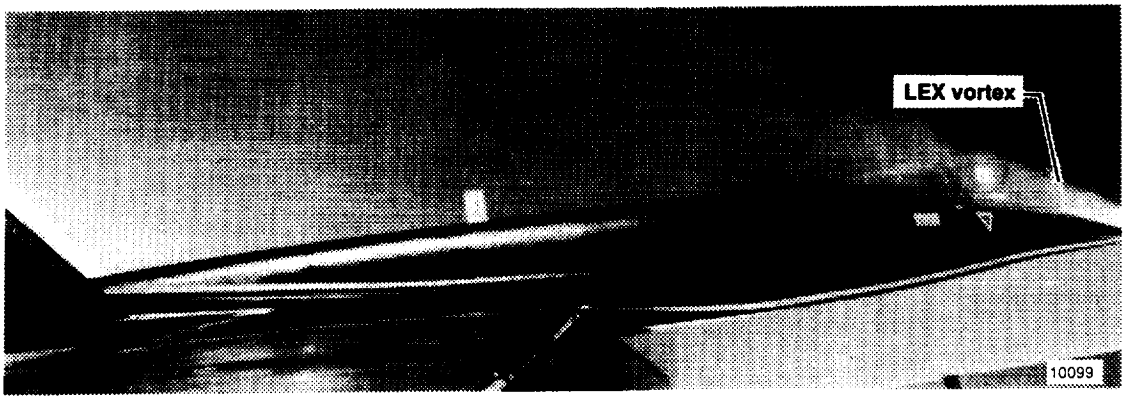

(f) $\alpha = 42.5°$ and $\beta = 0.9°$.

Figure 7. Concluded.

	$Re_{\bar{c}}$	Model scale, percent	Fluid medium	Ref.
● Flight	8 to 13 x 10^6	–	Air	15
□ DTRC	1.75 x 10^6	6	Air	4,15
◇ BART	1.60 x 10^5	3	Air	15
△ LSWT	3.60 x 10^5	12	Air	15
▱ FVF	1.26 x 10^4	3	Water	15

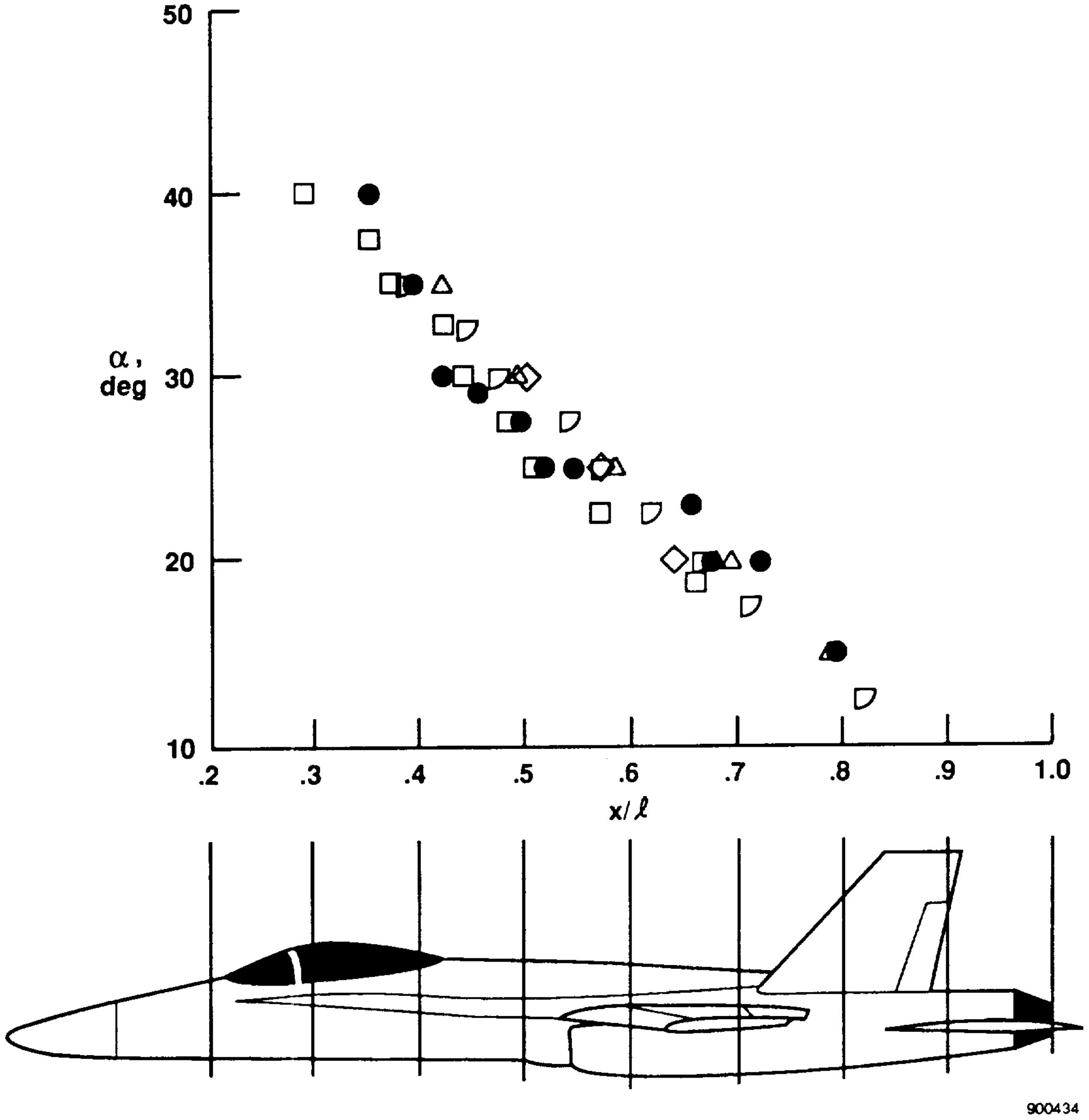

Figure 8. Comparison of F-18 LEX vortex core breakdown between flight and ground facilities.

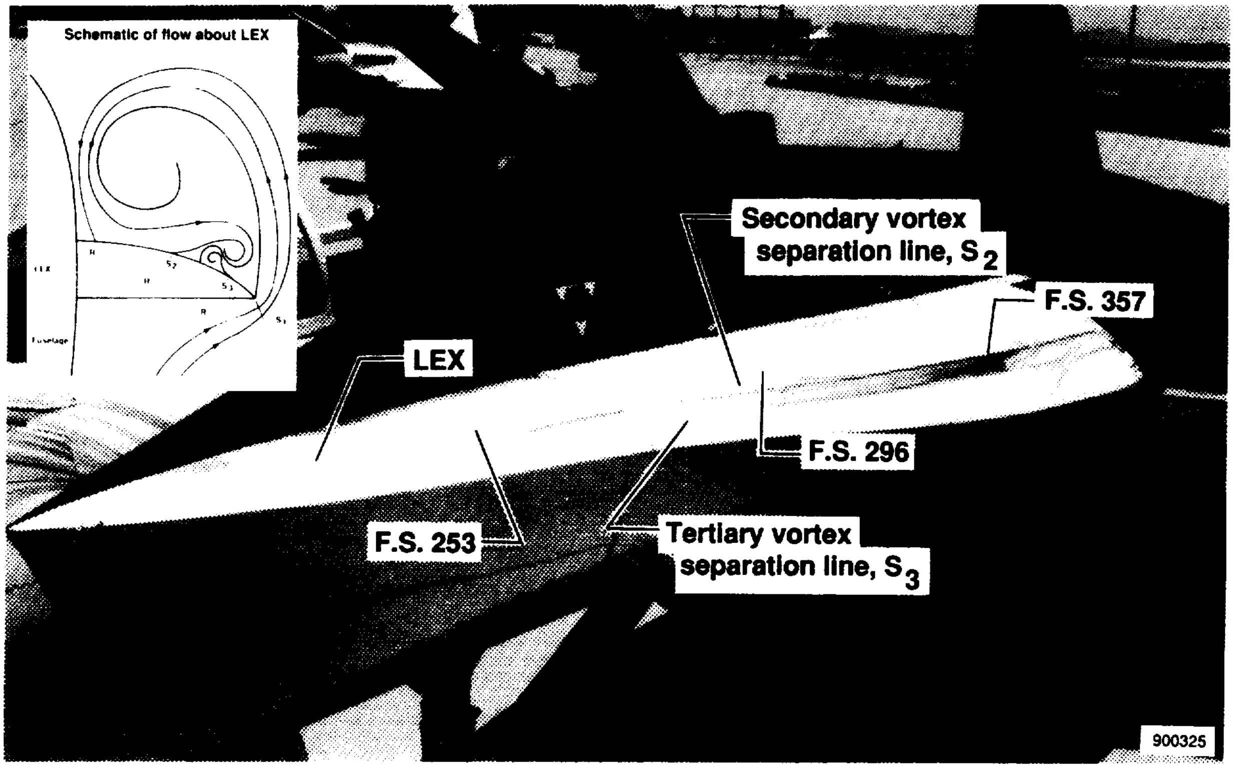

Figure 9. Surface flow visualization on left LEX of F-18 HARV for $\alpha \sim 30°$.

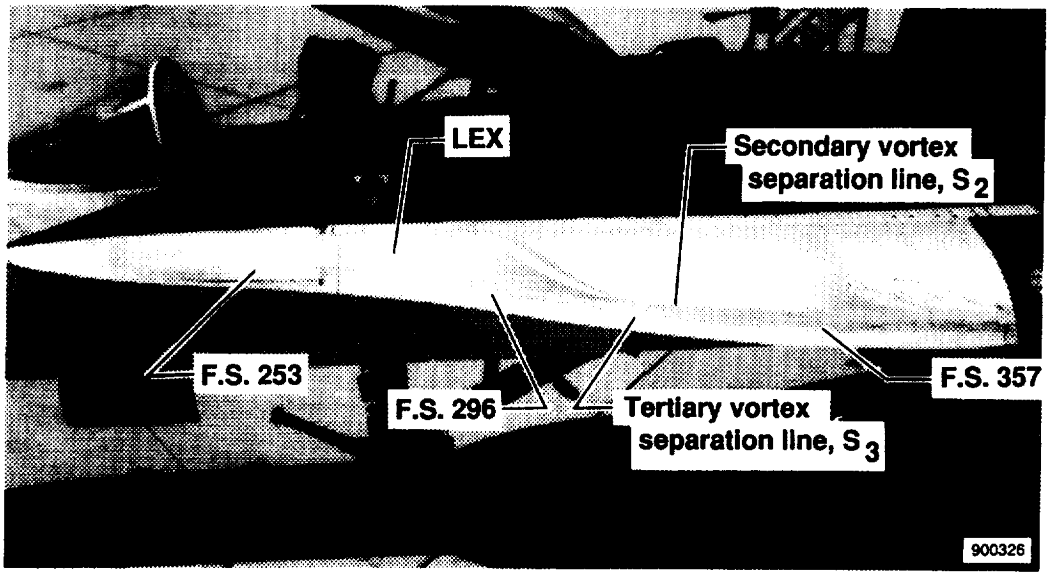

Figure 10. Surface flow visualization on left LEX of F-18 HARV for $\alpha \sim 47°$.

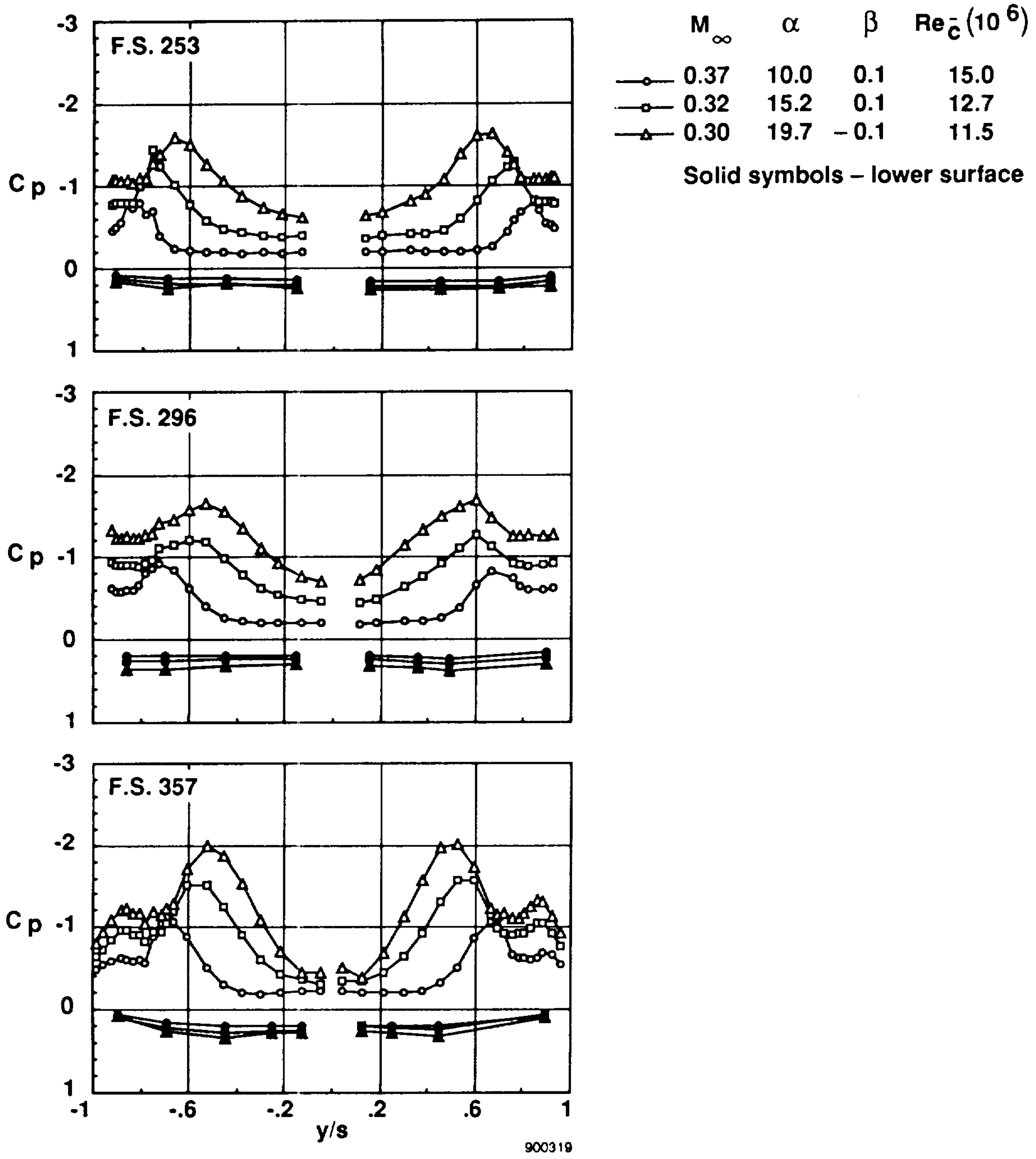

(a) α = 10.0°, 15.2°, and 19.7°; $M_\infty \sim 0.35$.

Figure 11. Effect of angle of attack on LEX surface static pressure coefficients on the F-18 HARV at low speed.

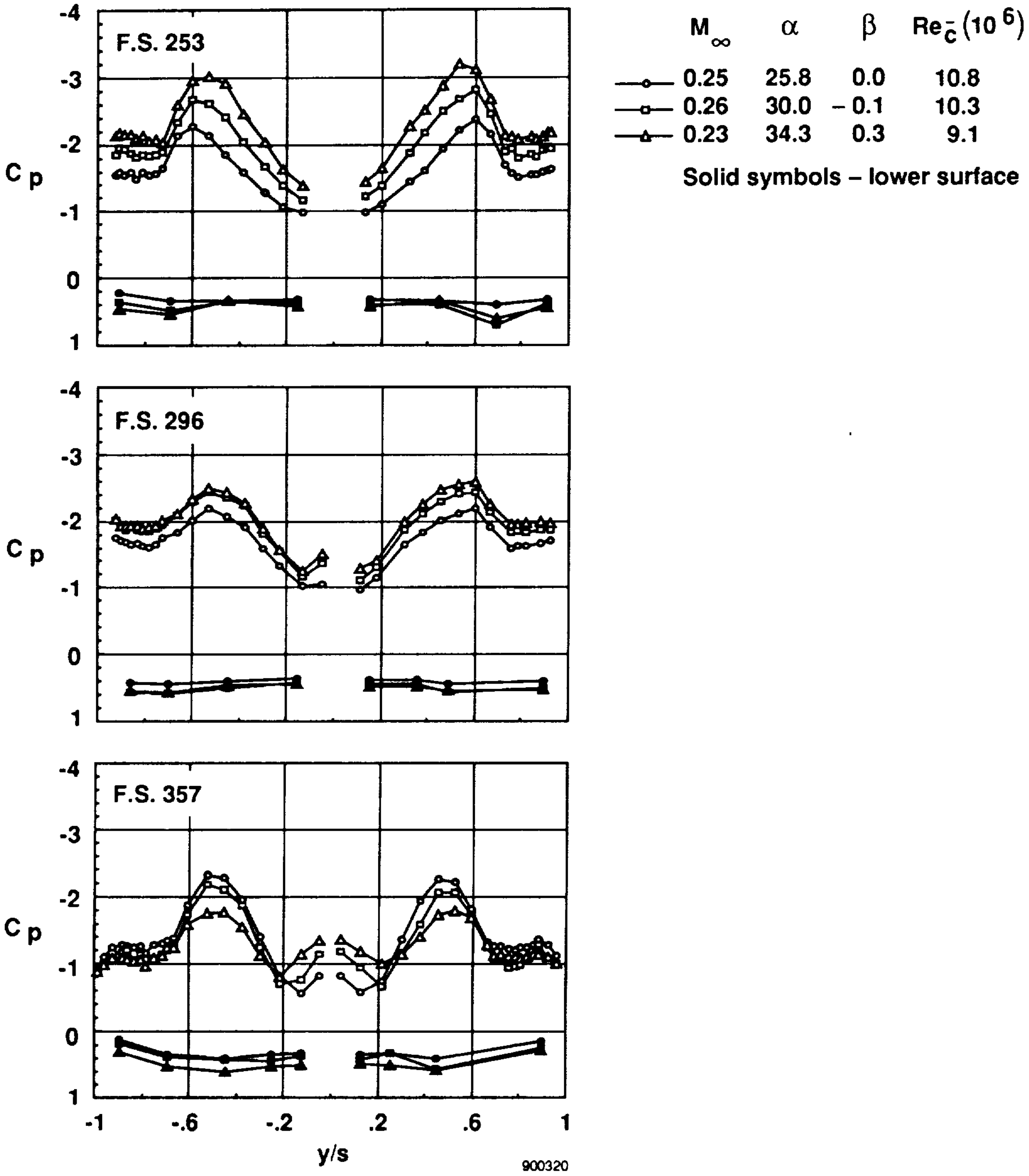

(b) $\alpha = 25.8°, 30.0°$, and $34.3°$; $M_\infty \sim 0.25$.

Figure 11. Continued.

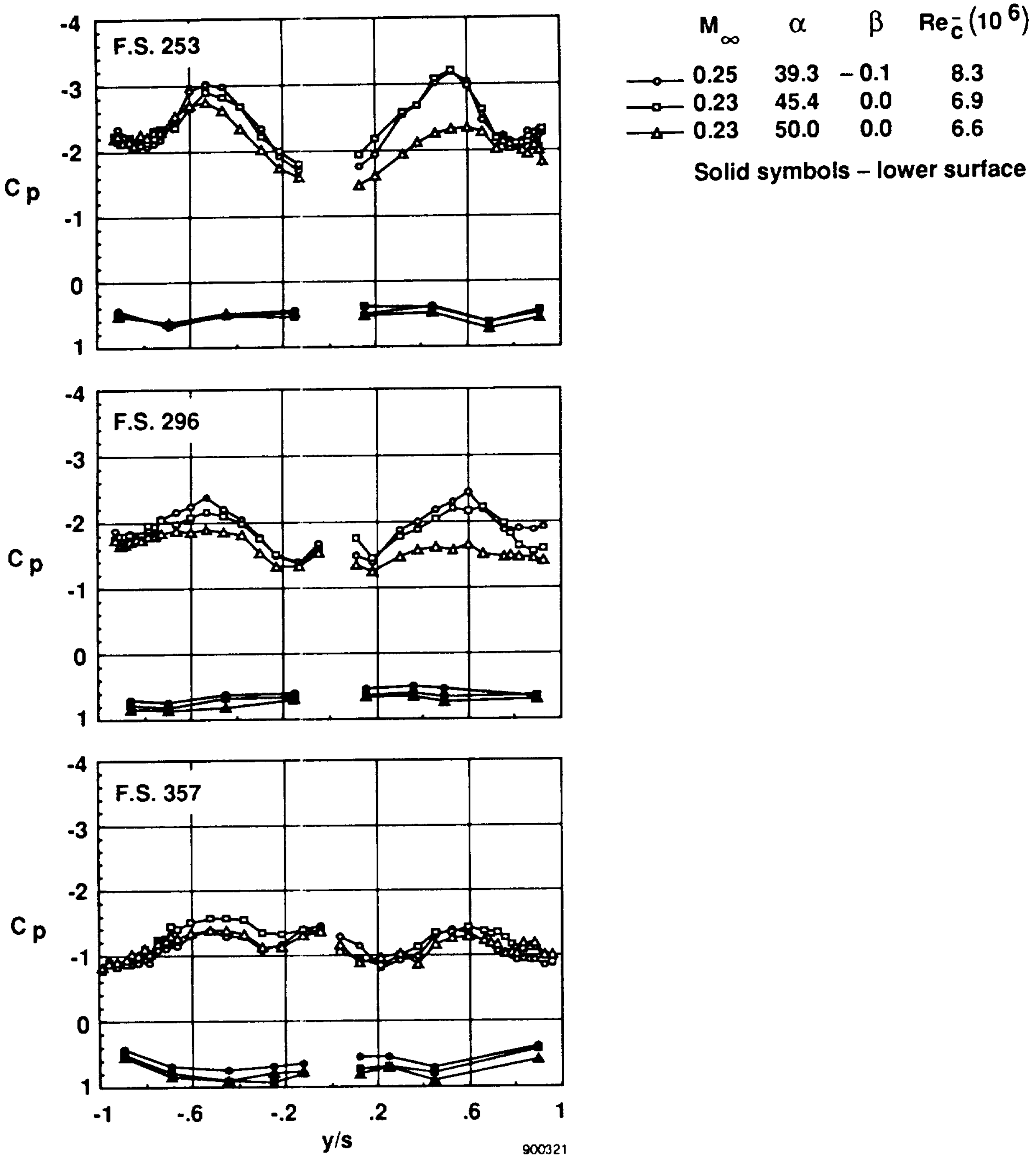

(c) α = 39.4°, 45.4°, and 50.0°; $M_\infty \sim 0.25$.

Figure 11. Concluded.

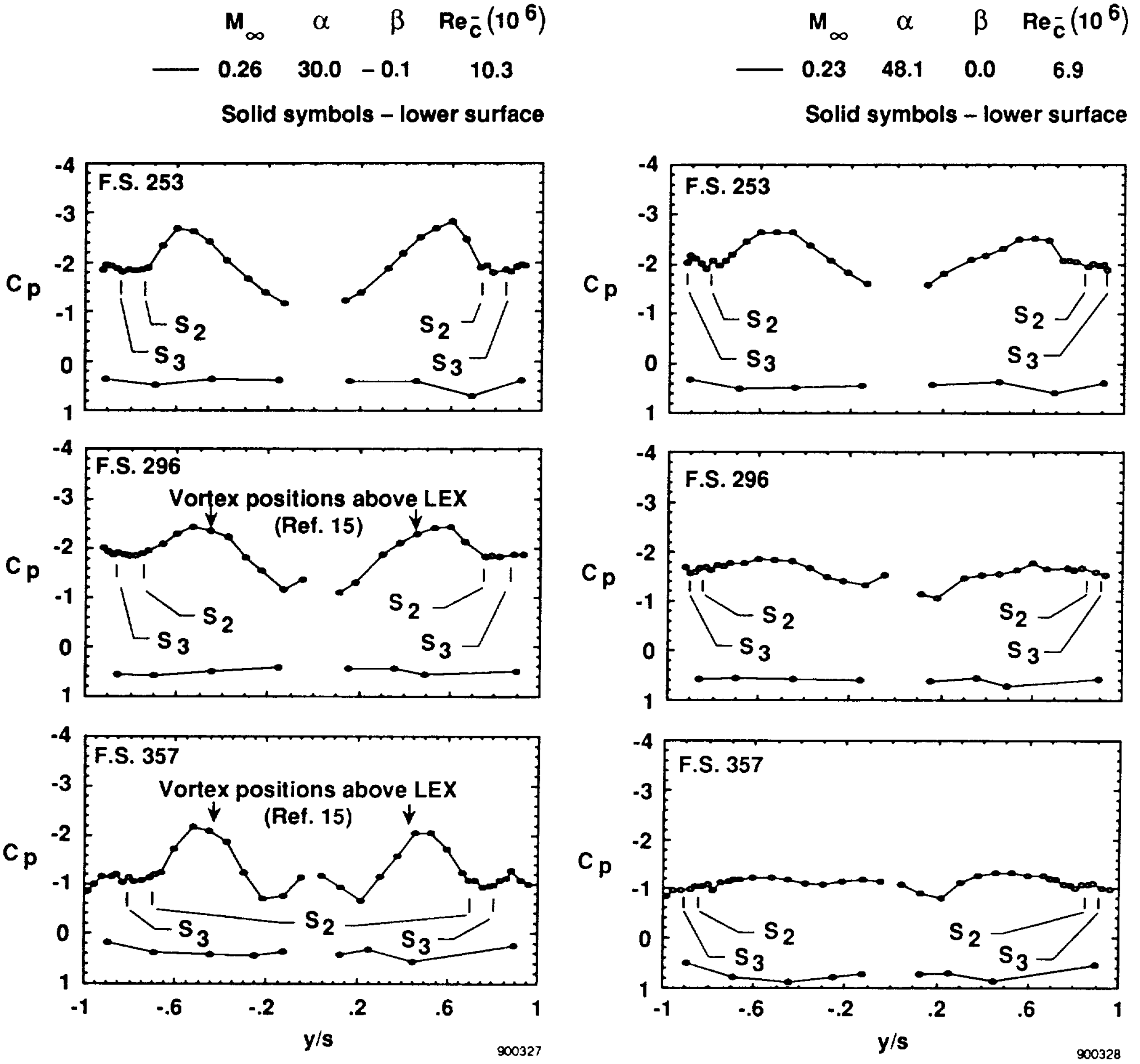

(a) $\alpha \approx 30°$.

(b) $\alpha \approx 48°$.

Figure 12. Comparison of LEX surface static pressure coefficients with flow visualization results on the F-18 HARV.

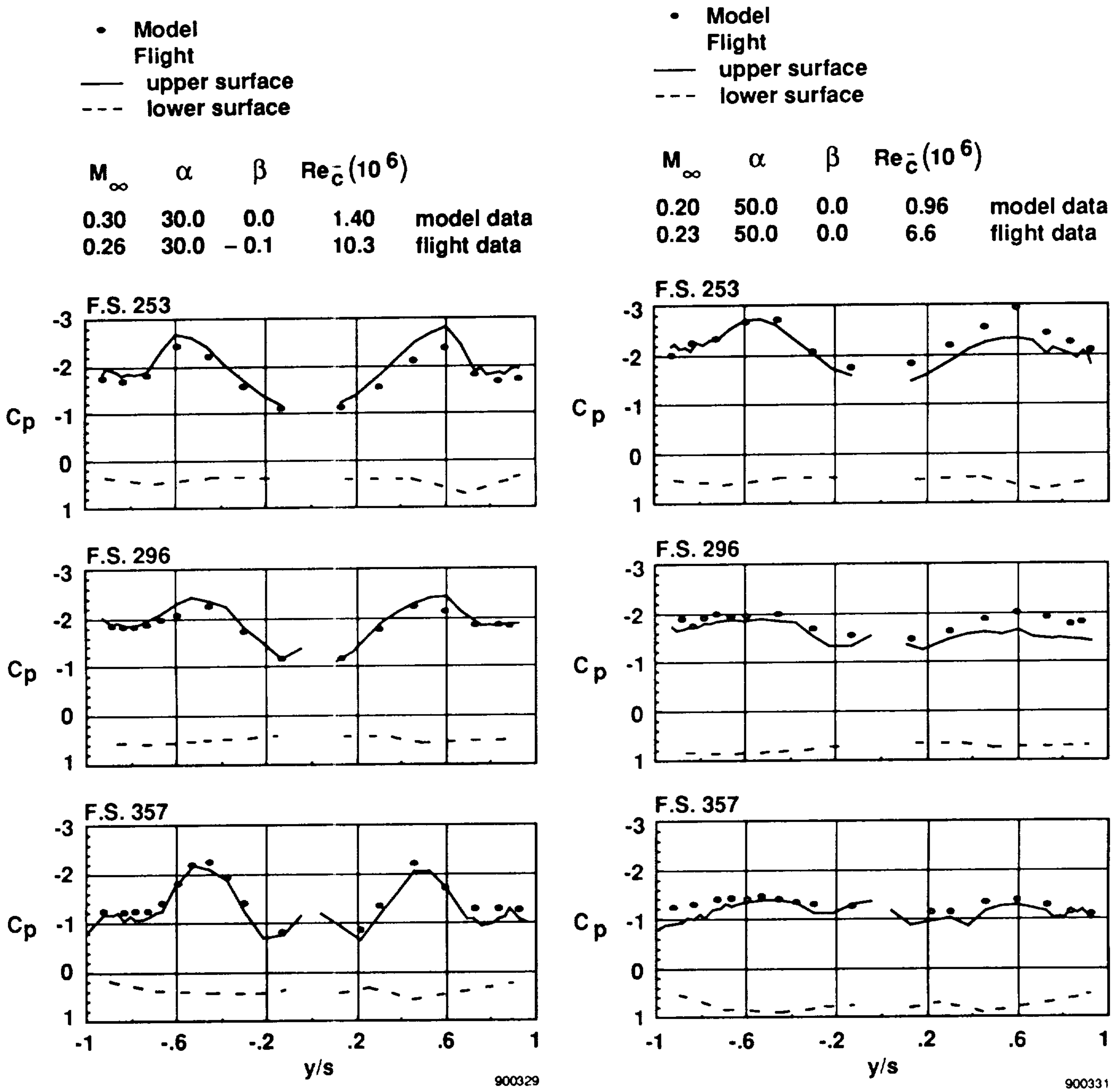

(a) $\alpha = 30.0^{\circ}$.

(b) $\alpha = 50.0^{\circ}$.

Figure 13. Comparison of flight- and wind-tunnel measured LEX surface static pressure coefficients on the F-18 HARV.

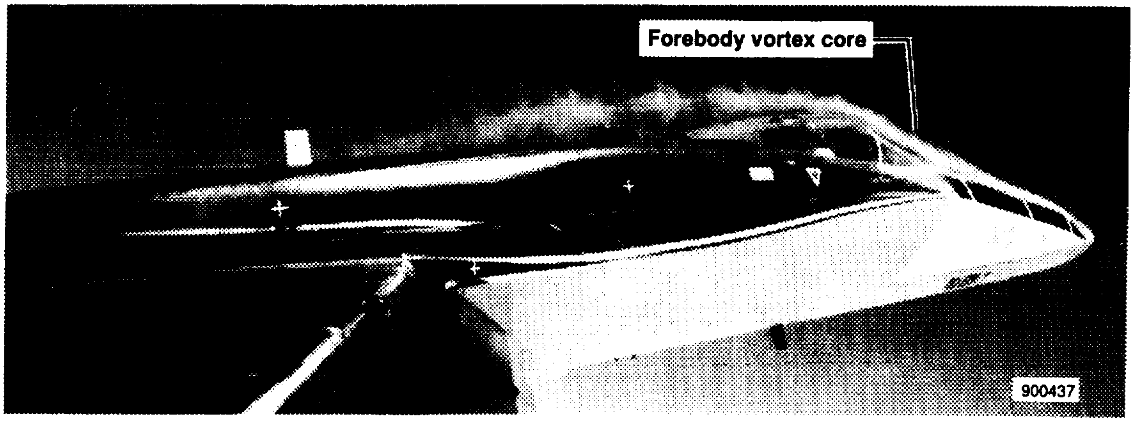

(a) $\alpha = 29.5°, \beta = 0.4°$.

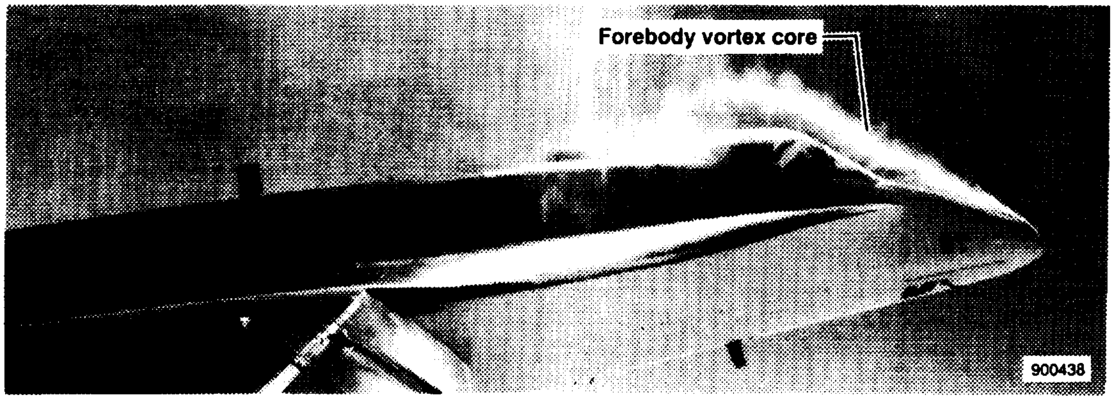

(b) $\alpha = 47.7°, \beta = 0.7°$.

Figure 14. Photographs from wingtip cameras of smoke entrained in forebody vortex core at two angles of attack.

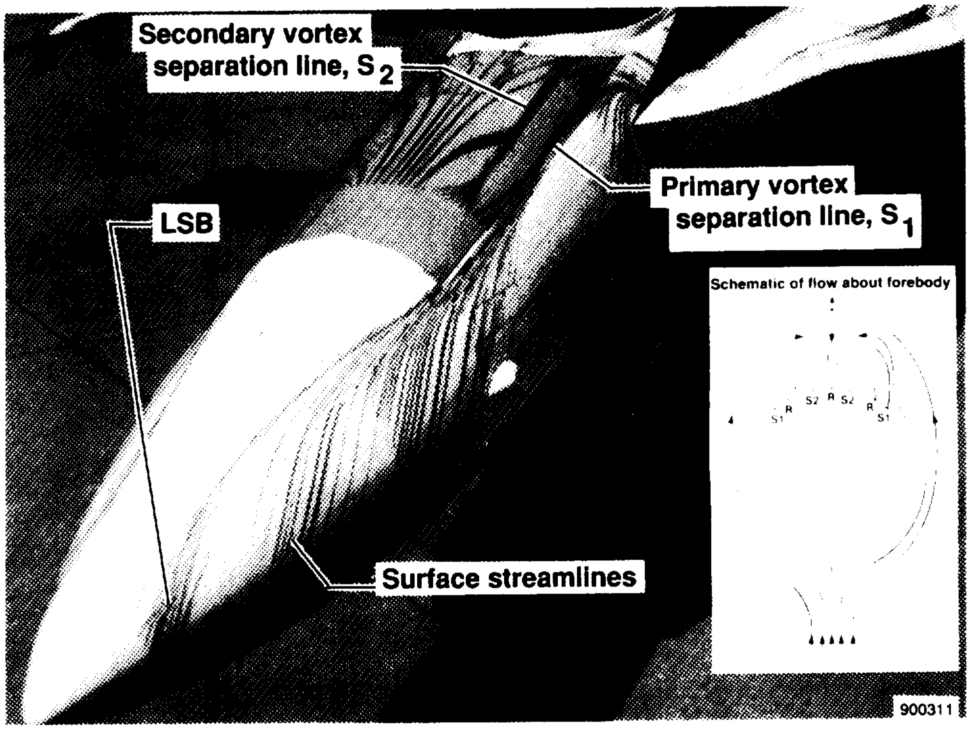

Figure 15. Surface flow visualization of F-18 HARV forebody for $\alpha \sim 30°$.

ORIGINAL PAGE
BLACK AND WHITE PHOTOGRAPH

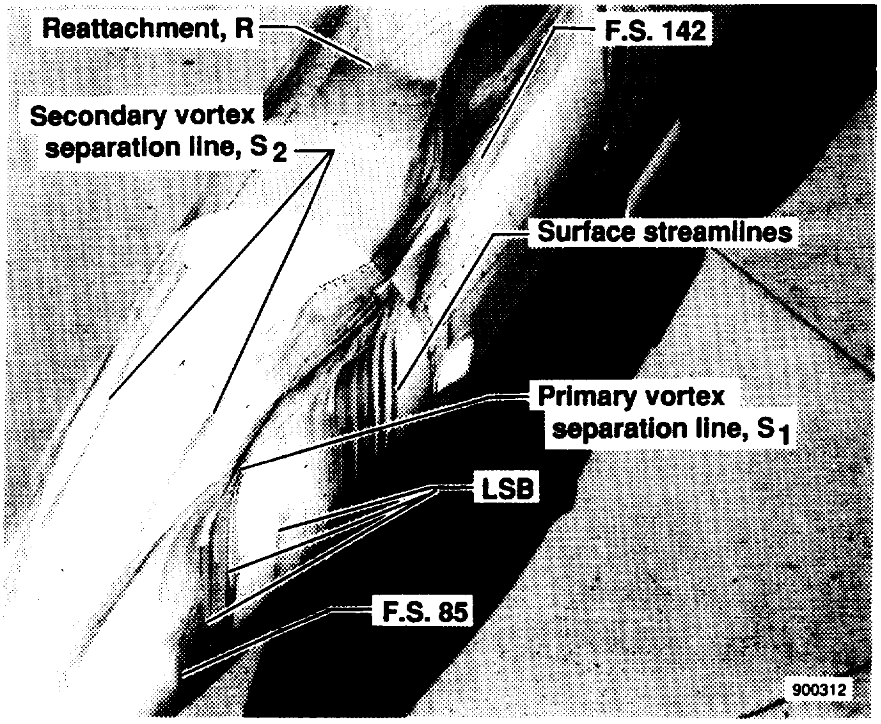

(a) 1/4 view.

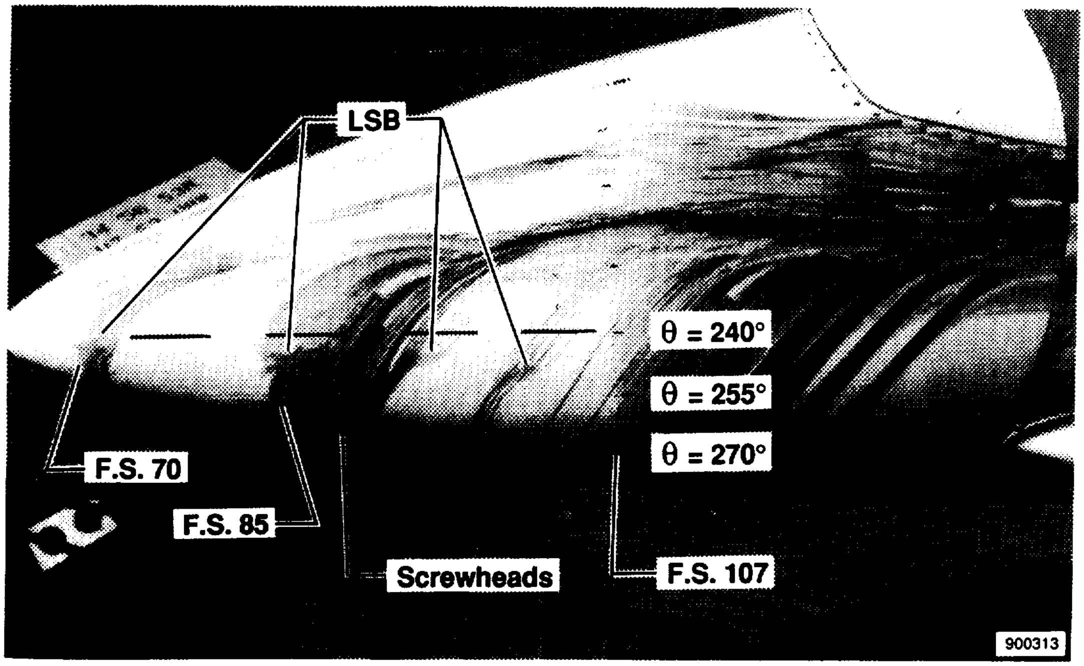

(b) Closeup of nosecone.

Figure 16. Surface flow visualization on F-18 HARV forebody for $\alpha \sim 47°$.

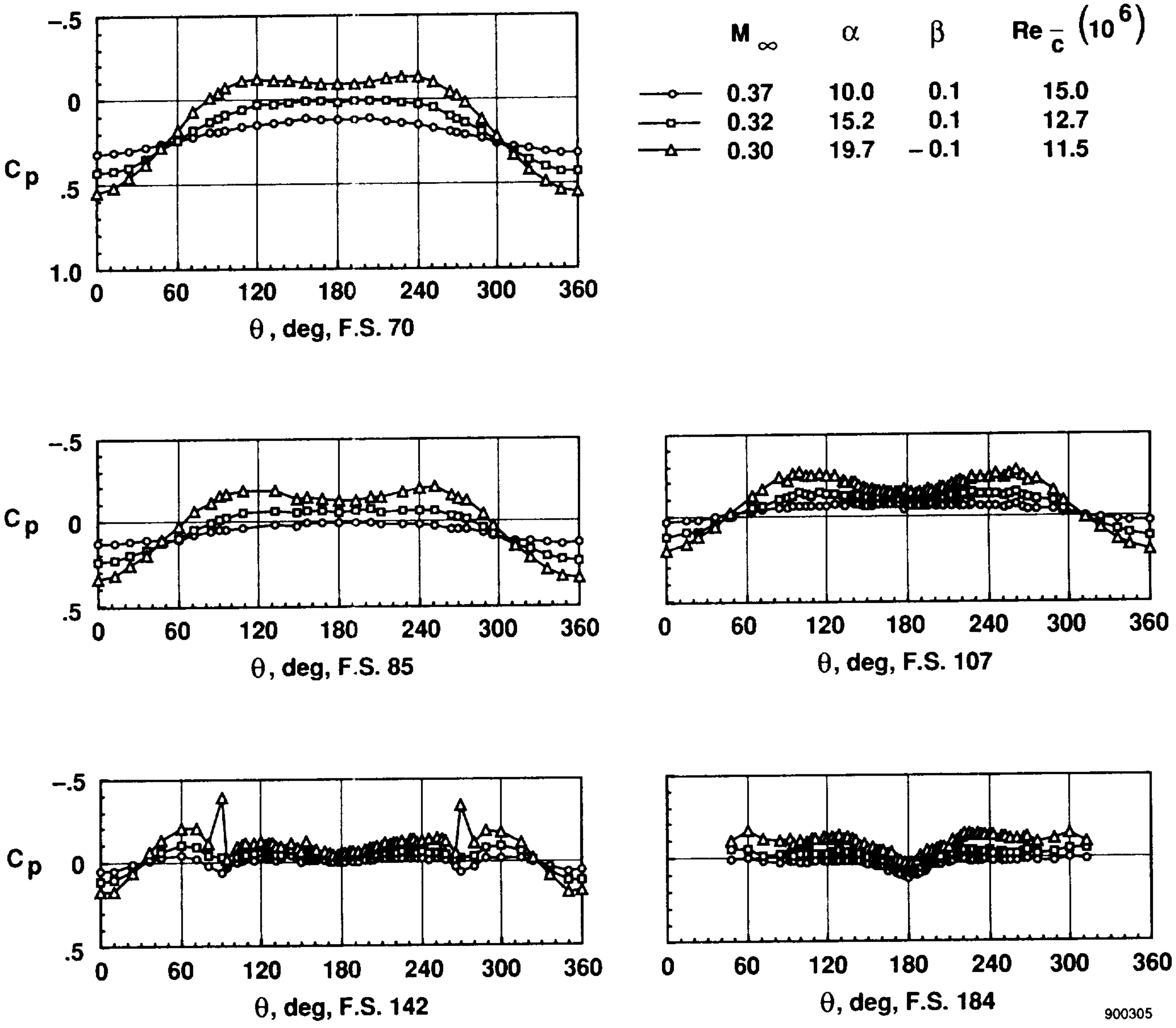

(a) $\alpha = 10.0°, 15.2°$, and $19.7°$; $M_\infty \sim 0.35$.

Figure 17. Effect of angle of attack on forebody surface static pressure coefficient on the F-18 HARV at low speed.

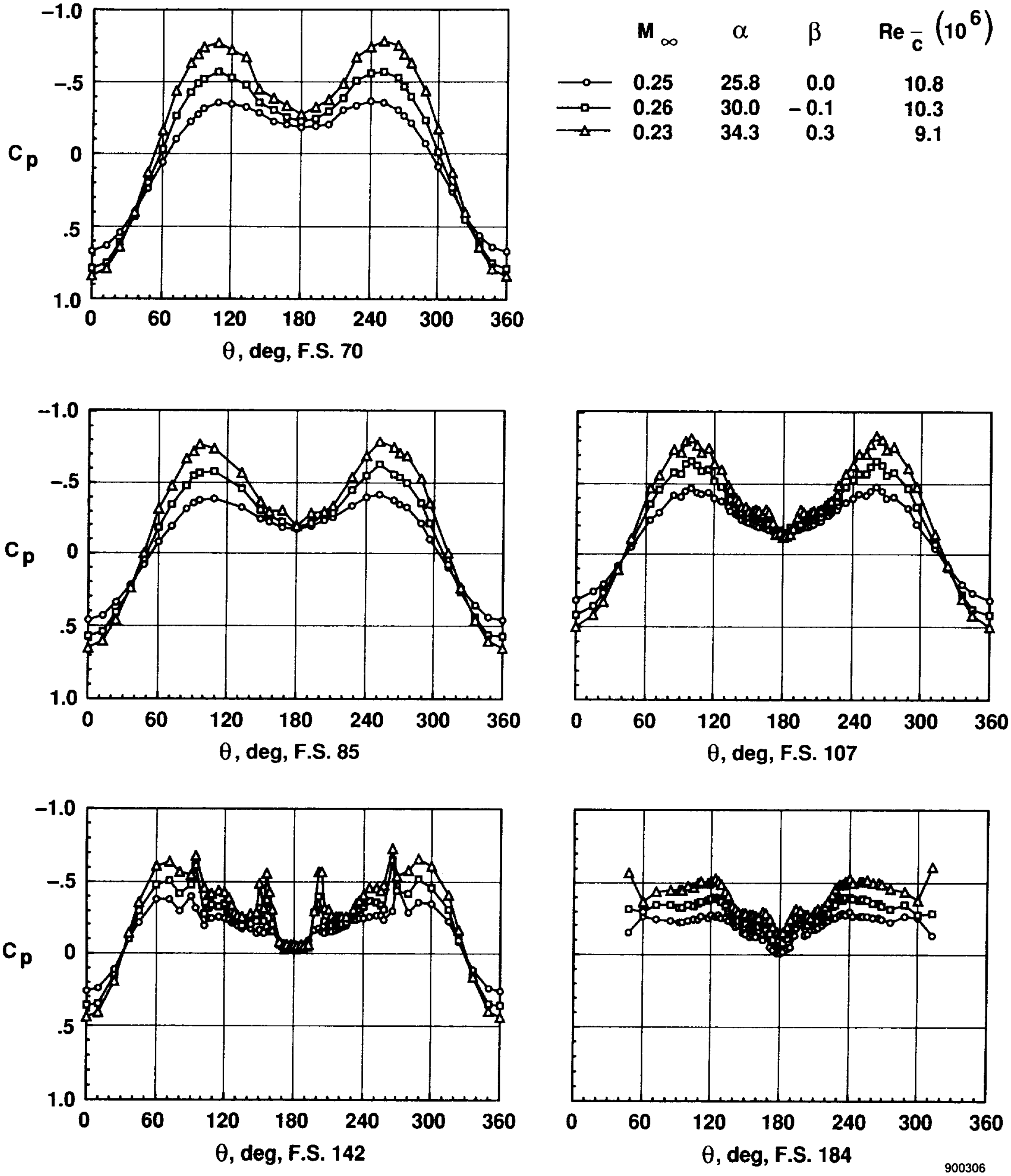

(b) $\alpha = 25.8°$, 30.0°, and 34.3°; $M_\infty \sim 0.25$.

Figure 17. Continued.

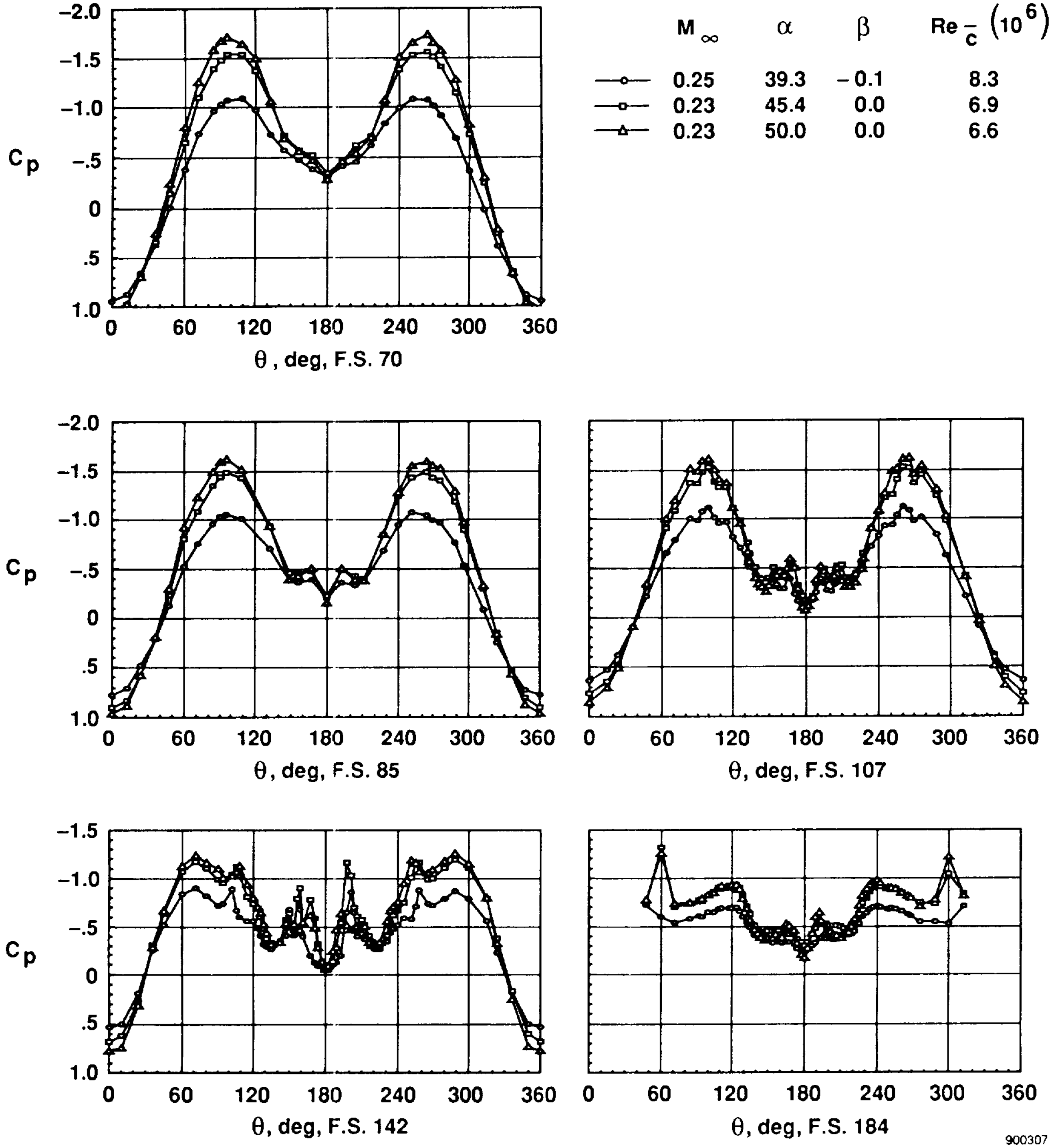

(c) α = 39.3°, 45.4°, and 50.0°; $M_\infty \sim 0.25$.

Figure 17. Concluded.

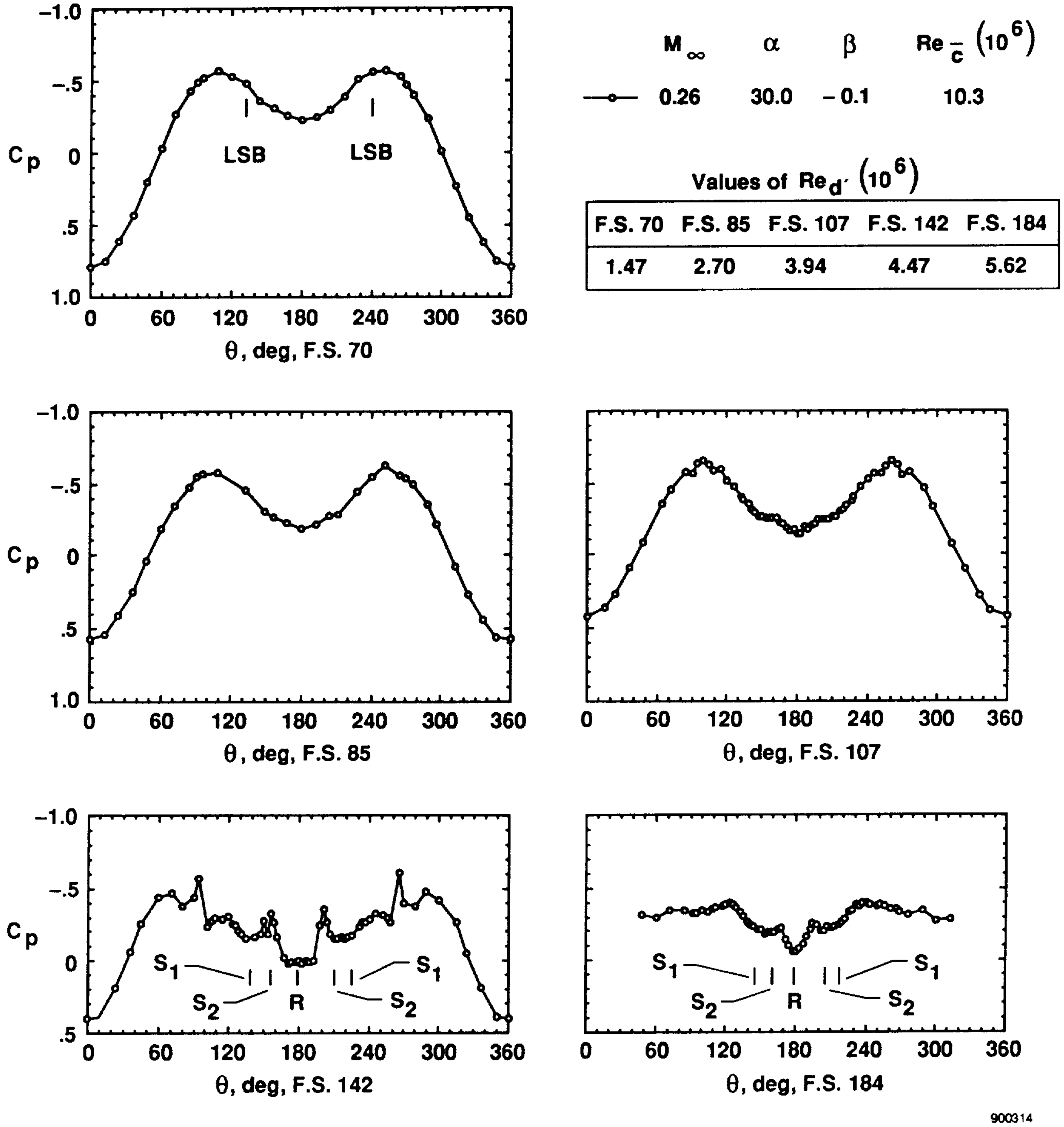

(a) $\alpha \approx 30.0°$.

Figure 18. Comparison of forebody surface static pressure coefficients with flow visualization results on the F-18 HARV.

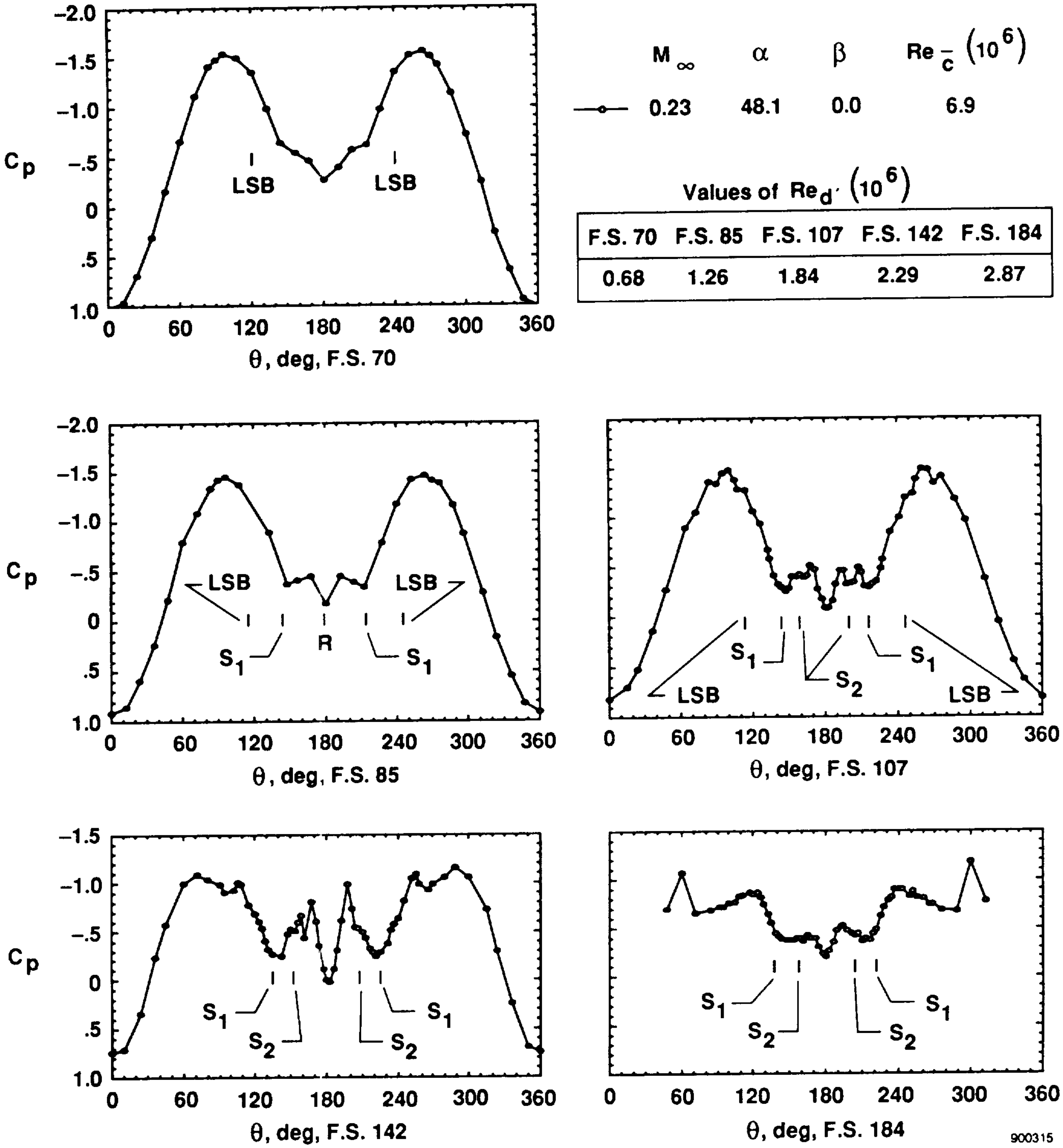

Values of $Re_{d'}$ (10^6)

F.S. 70	F.S. 85	F.S. 107	F.S. 142	F.S. 184
0.68	1.26	1.84	2.29	2.87

(b) $\alpha \approx 48°$.

Figure 18. Concluded.

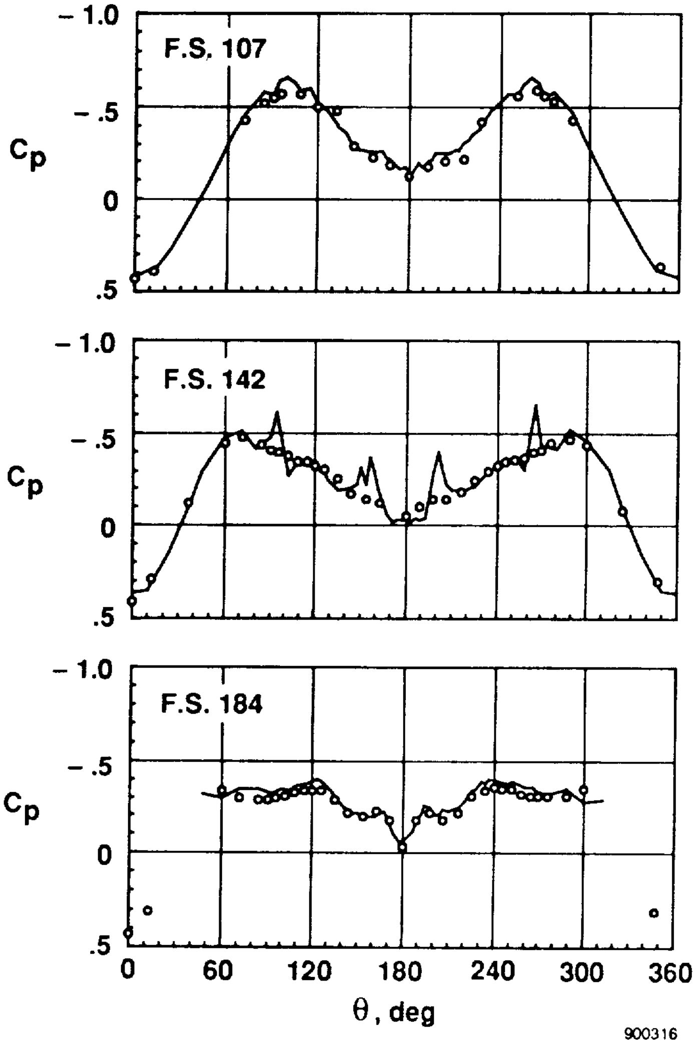

Values of $Re_d \cdot (10^6)$

	F.S. 107	F.S. 142	F.S. 184
Model	0.54	0.61	0.76
Flight	3.94	4.47	5.62

	M_∞	α	β	$Re_{\bar{c}} (10^6)$
○ Model	0.30	30.0	0.0	1.40
—— Flight	0.26	30.0	- 0.1	10.3

900316

(a) $\alpha = 30.0°$.

Figure 19. Comparison of flight- and wind-tunnel measured surface static pressure coefficients on the F-18 HARV forebody.

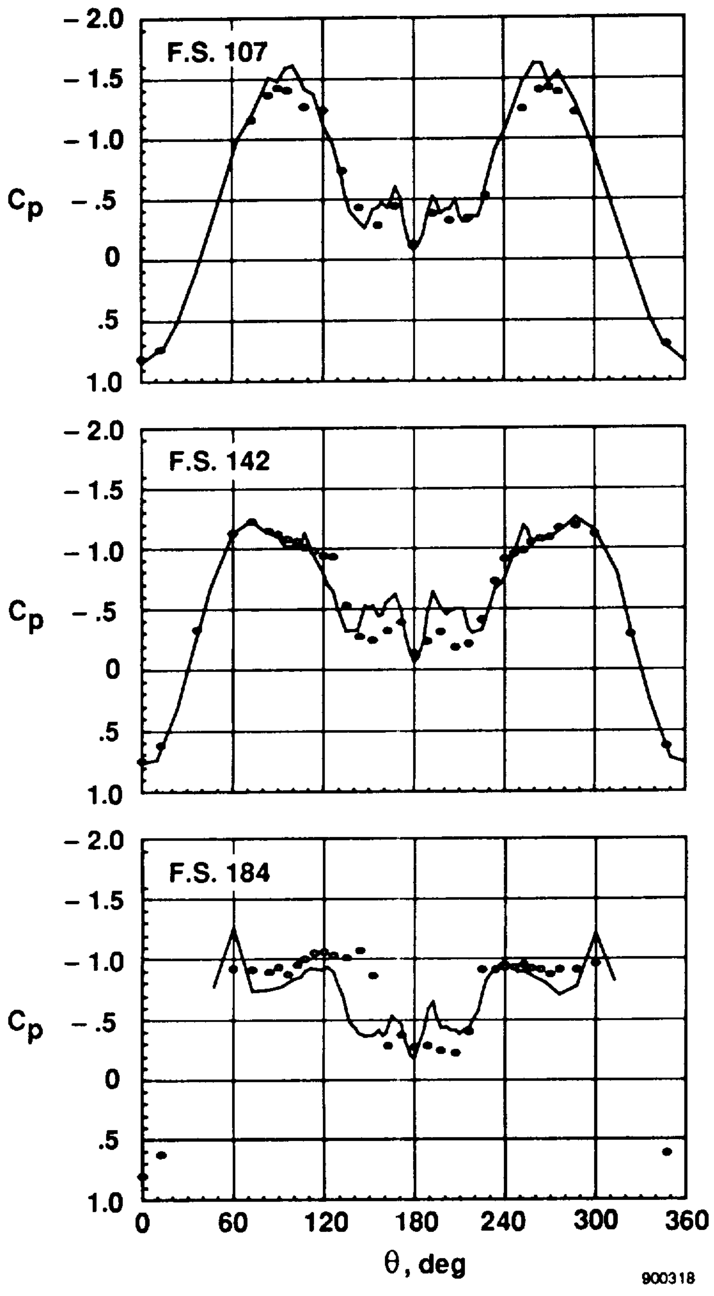

Values of $Re_{d'}(10^6)$

	F.S. 107	F.S. 142	F.S. 184
Model	0.25	0.31	0.39
Flight	1.72	2.15	2.70

	M_∞	α	β	$Re_{\bar{c}}(10^6)$
● Model	0.20	50.0	0.0	0.96
—— Flight	0.23	50.0	0.0	6.6

(b) $\alpha = 50.0°$.

Figure 19. Concluded.

ORIGINAL PAGE
BLACK AND WHITE PHOTOGRAPH

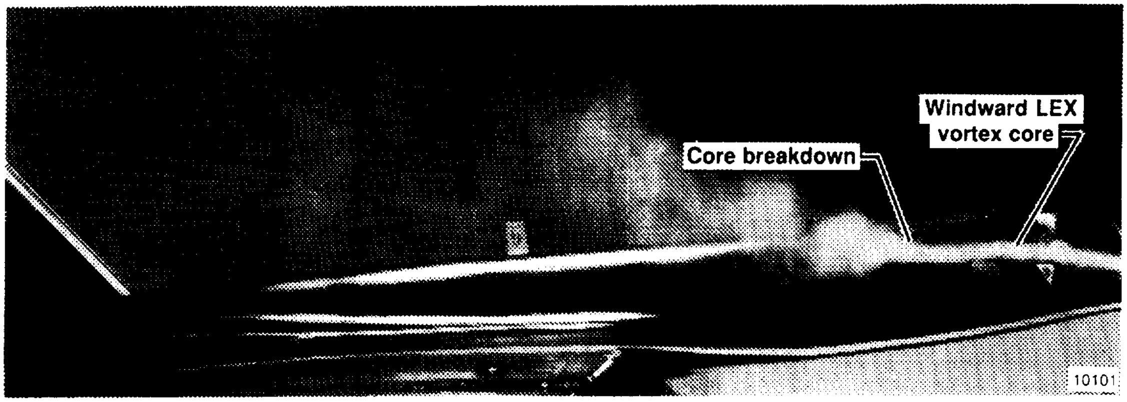

(a) $\alpha = 26°$ and $\beta = 4.52°$.

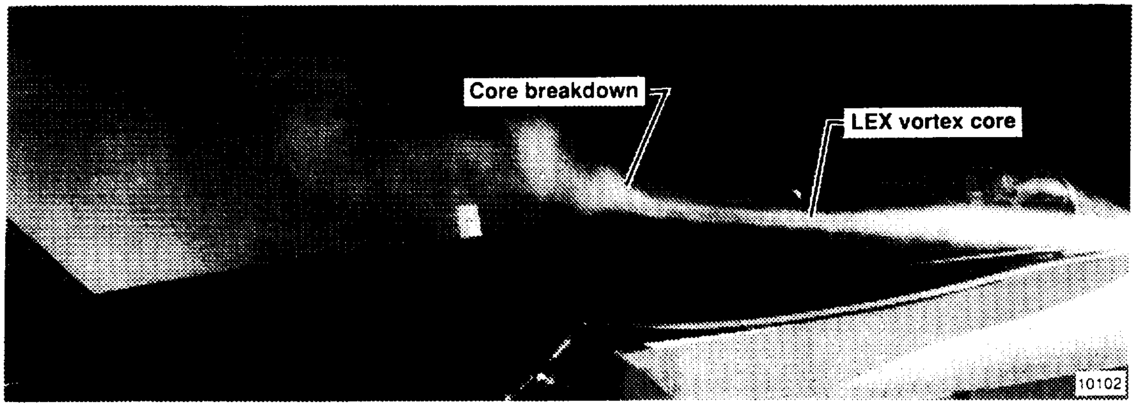

(b) $\alpha = 25°$ and $\beta = 1°$.

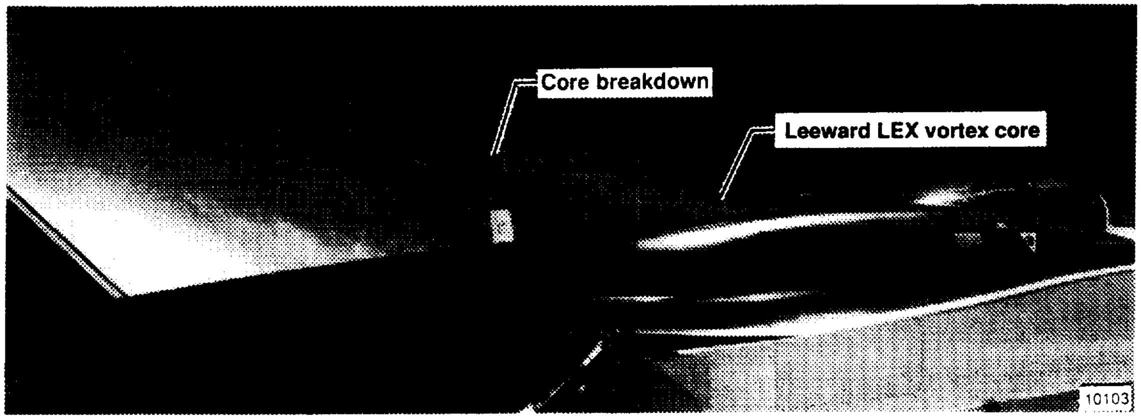

(c) $\alpha = 24.7°$ and $\beta = -3.4°$.

Figure 20. Right wingtip view showing effects of increased angle of sideslip on LEX vortex core and breakdown point.

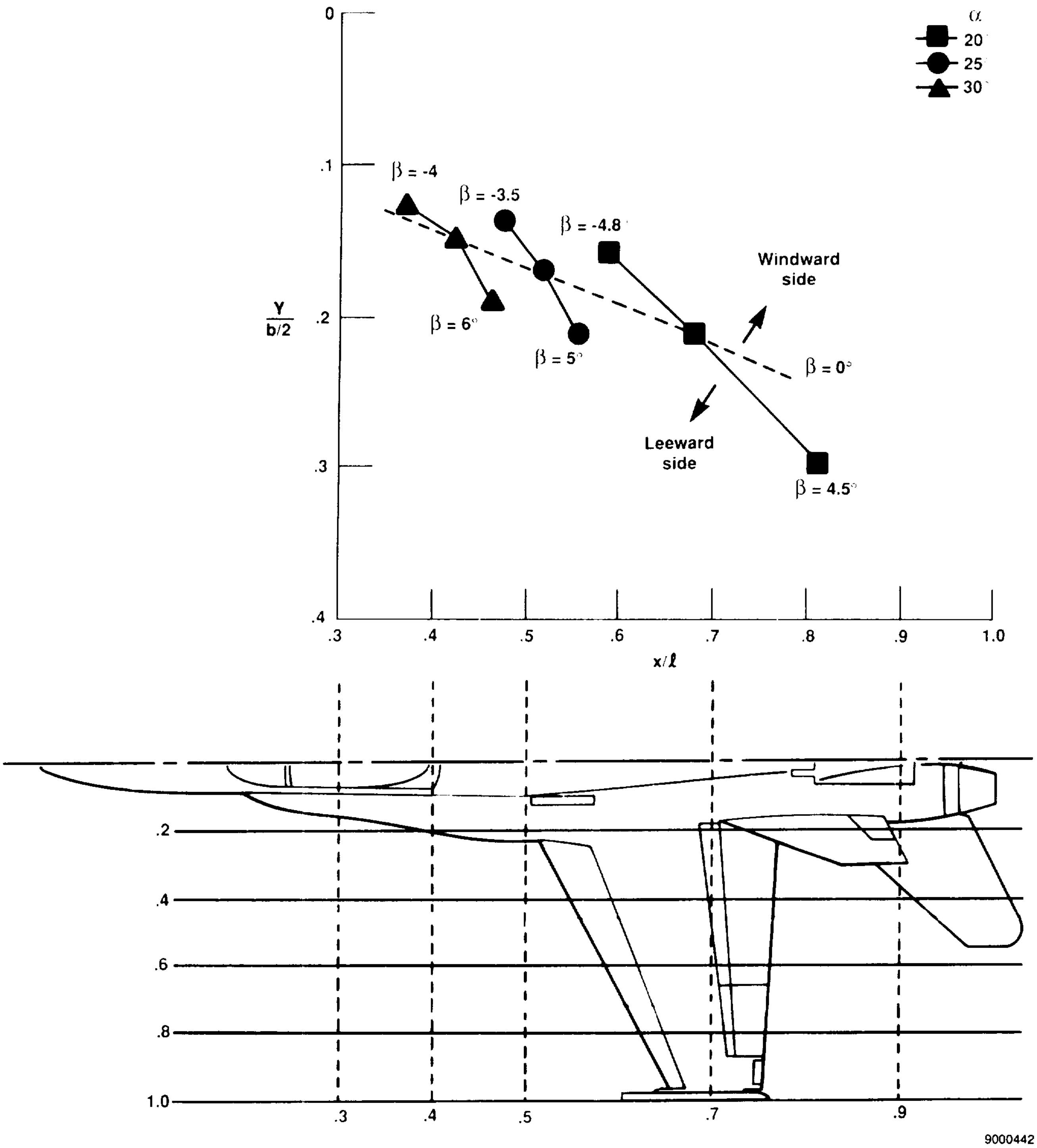

Figure 21. Comparison of left F-18 LEX vortex core breakdown location for a range of angle of sideslip and angle of attack.

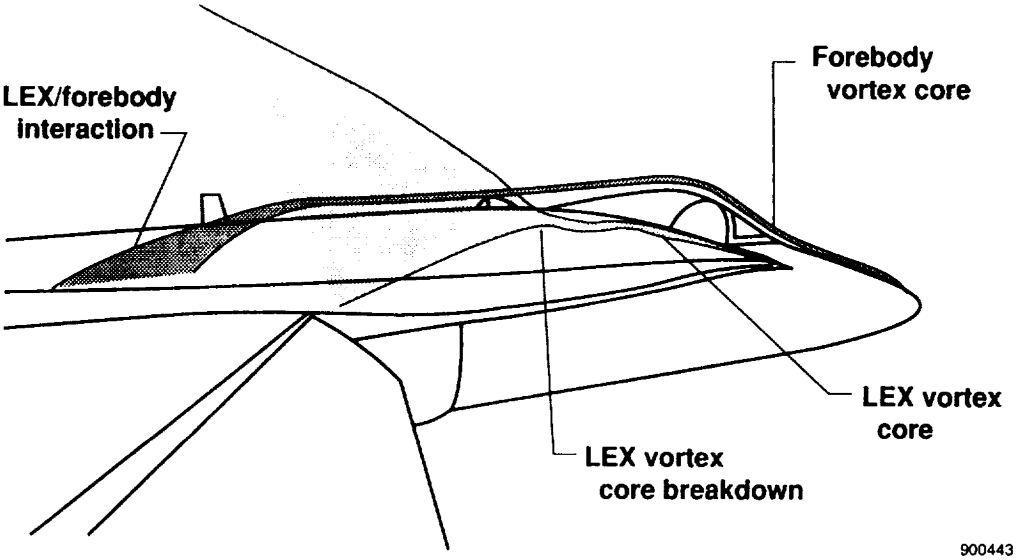

ORIGINAL PAGE
BLACK AND WHITE PHOTOGRAPH

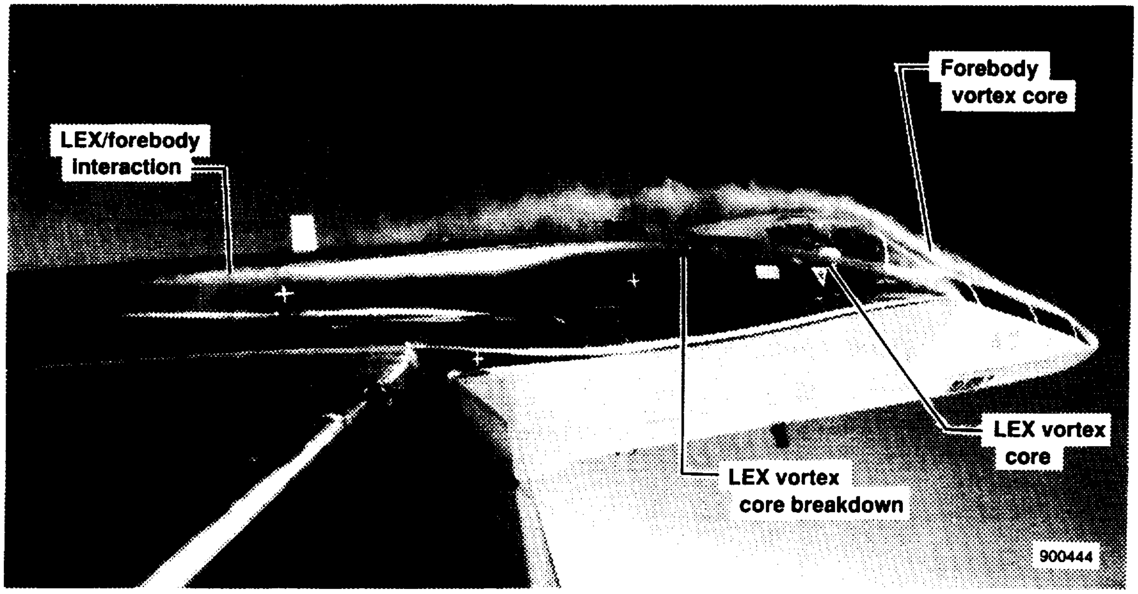

(a) $\alpha = 29.5°$ and $\beta = 0.4°$.

Figure 22. Wingtip view of forebody vortex system.

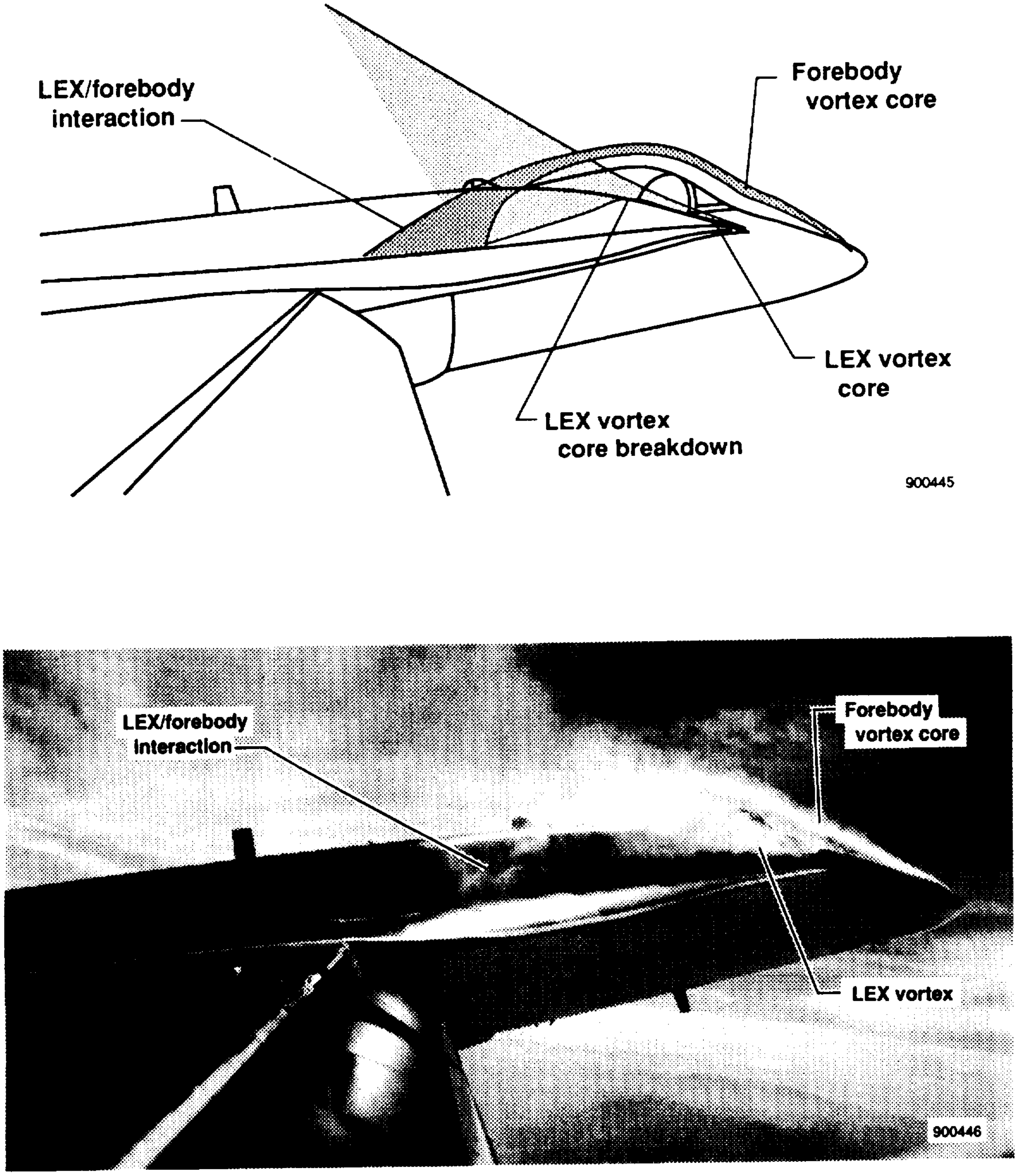

(b) $\alpha = 38.7°$ and $\beta = 0°$.

Figure 22. Continued.

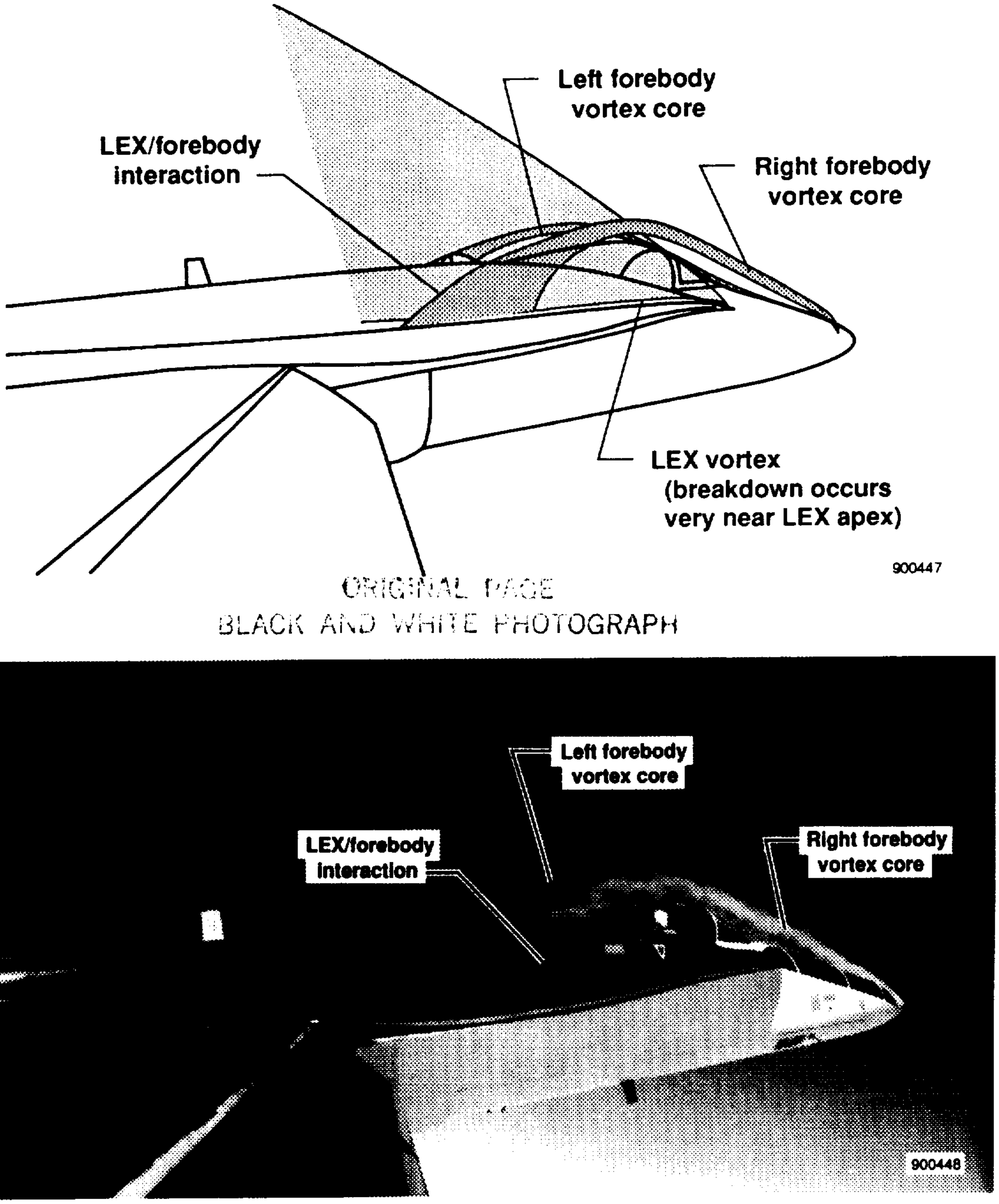

(c) $\alpha = 42.5°$ and $\beta = -0.5°$.

Figure 22. Concluded.

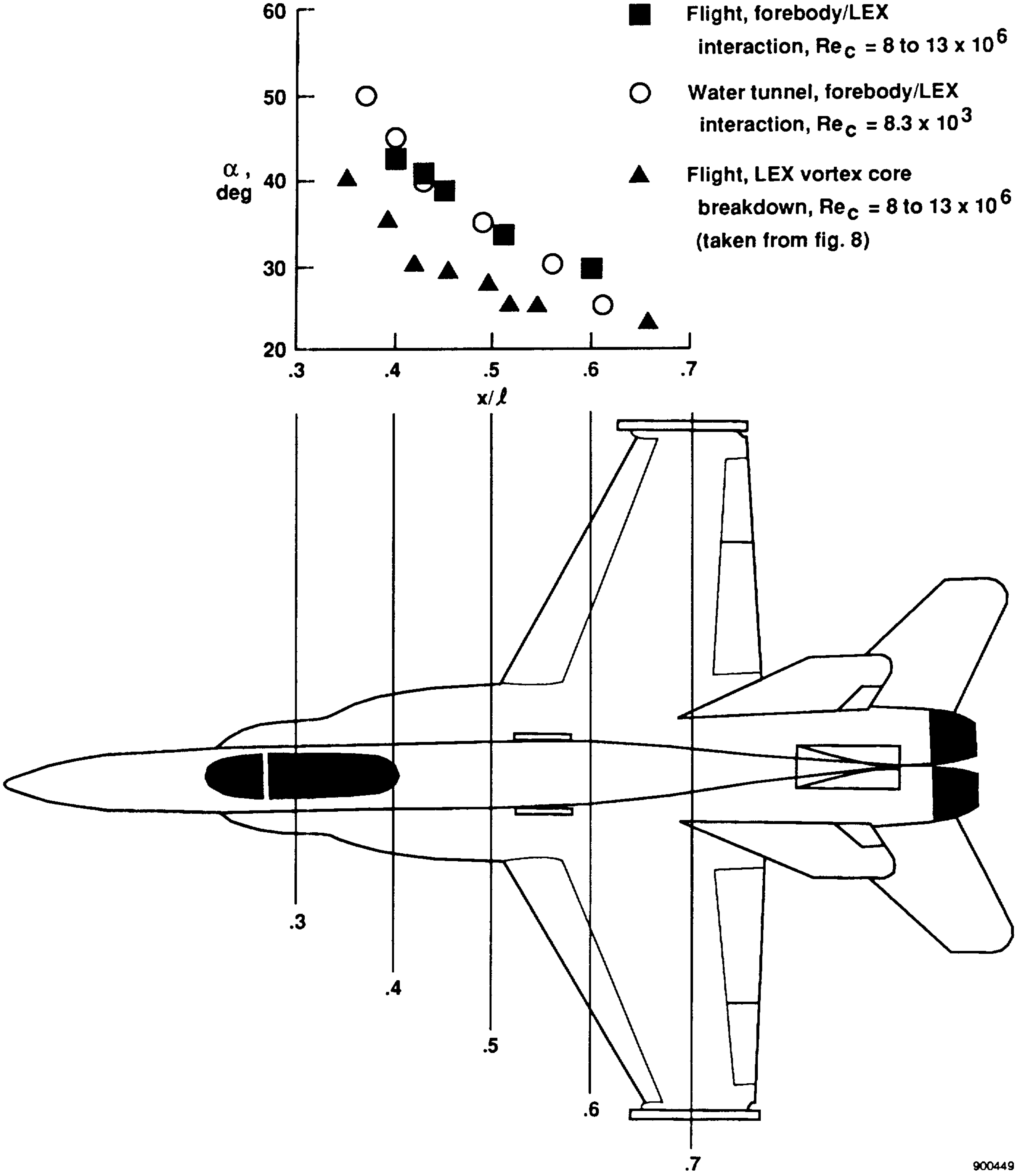

Figure 23. Longitudinal location of LEX vortex core breakdown and of forebody and LEX vortex interaction for various angles of attack, $\beta = 0°$.

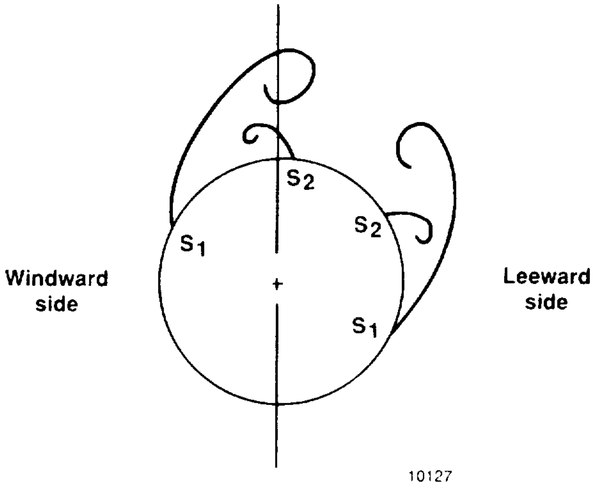

Figure 24. Cross sectional view of forebody vortex system at sideslip.

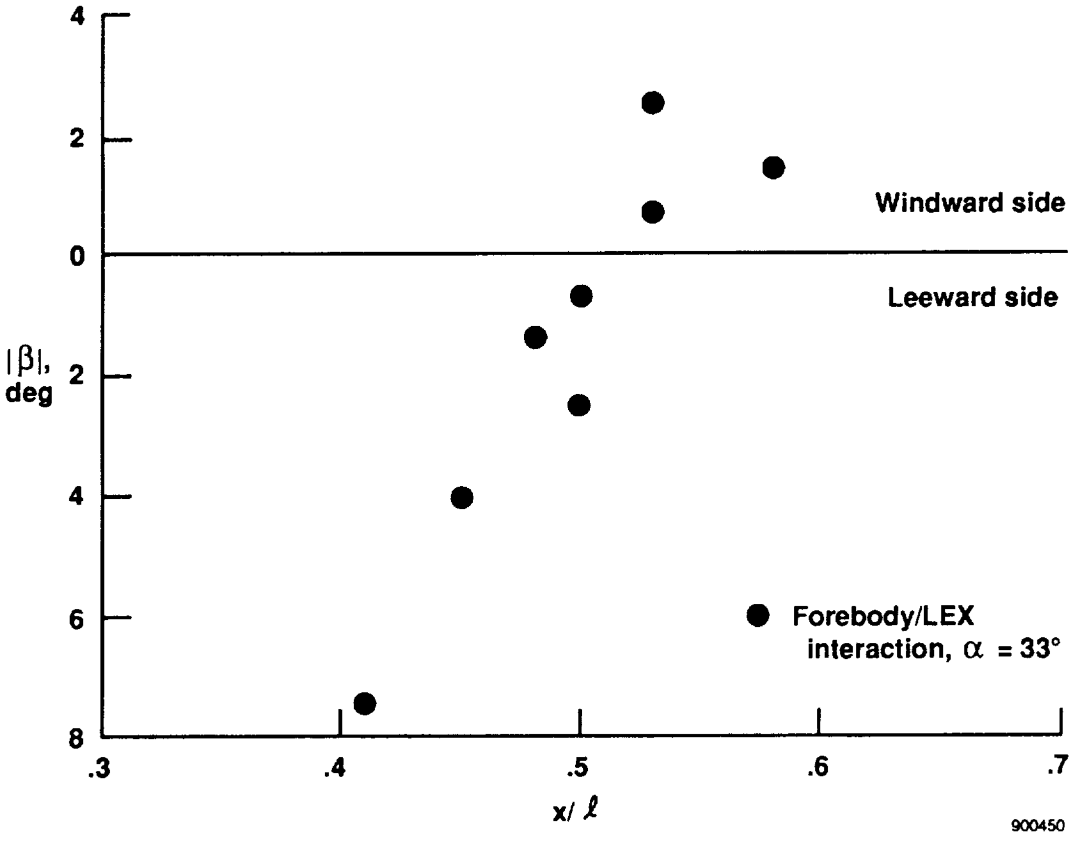

Figure 25. Flight measured location of forebody/LEX vortex interaction as a function of sideslip, $\alpha = 33^\circ$.

National Aeronautics and Space Administration

Report Documentation Page

1. Report No.
NASA TM-101726

2. Government Accession No.

3. Recipient's Catalog No.

4. Title and Subtitle
In-Flight Flow Visualization with Pressure Measurements at Low Speeds on the NASA F-18 High Alpha Research Vehicle

5. Report Date
October 1990

6. Performing Organization Code

7. Author(s)
John H. Del Frate, David F. Fisher, and Fanny A. Zuniga

8. Performing Organization Report No.
H-1651

10. Work Unit No.
RTOP 505-68-71

9. Performing Organization Name and Address
NASA Ames Research Center
Dryden Flight Research Facility
P.O. Box 273, Edwards, CA 93523-0273

11. Contract or Grant No.

13. Type of Report and Period Covered
Technical Memorandum

12. Sponsoring Agency Name and Address
National Aeronautics and Space Administration
Washington, DC 20546-0001

14. Sponsoring Agency Code

15. Supplementary Notes

Prepared as a conference paper for presentation at the AGARD Vortex Flow Aerodynamics Conference, Scheveningen, Netherlands, October 1–4, 1990.

16. Abstract

In-flight results from surface and off-surface flow visualizations and from extensive pressure distributions document the vortical flow on the leading-edge extensions (LEXs) and forebody of the NASA F-18 high alpha research vehicle (HARV) for low speeds and angles of attack up to 50°. Surface flow visualization data, obtained using the emitted fluid technique, were used to define separation lines and laminar separation bubbles (LSB). Off-surface flow visualization data, obtained by smoke injection, were used to document both the path of the vortex cores and the location of vortex core breakdown. The location of vortex core breakdown correlated well with the loss of suction pressure on the LEX and with the flow visualization results from ground facilities. Surface flow separation lines on the LEX and forebody corresponded well with the end of pressure recovery under the vortical flows. Correlation of the pressures with wind-tunnel results show fair to good correlation.

17. Key Words (Suggested by Author(s))
F-18, flight test, flow visualization, high angle of attack, low speed, vortex flow

18. Distribution Statement
Unclassified-Unlimited

Subject category - 02

19. Security Classif. (of this report)	20. Security Classif. (of this page)	21. No. of Pages	22. Price
Unclassified	Unclassified	42	A03

NASA FORM 1626 OCT 86

For sale by the National Technical Information Service, Springfield, Virginia 22161